NAVAL POSTGRADUATE SCHOOL
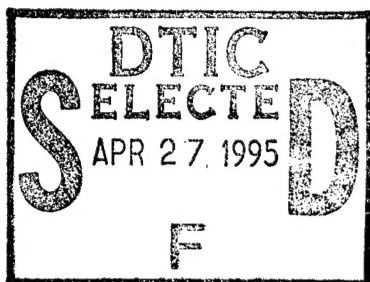## Monterey, California

DTIC
SELECTED
APR 27 1995
F

UNITED STATES NAVY
· NAVAL POSTGRADUATE SCHOOL ·

THESIS

COMPARISON OF SATELLITE-DERIVED MSU BRIGHTNESS TEMPERATURES AND CONVENTIONALLY-DERIVED FIELDS

by

Matthew C. Parke

December 1994

Thesis Co-Advisors: Paul A. Hirschberg
                                       Carlyle H. Wash

Approved for public release; distribution is unlimited

19950426 116

REPORT DOCUMENTATION PAGE

Form Approved OMB No. 0704-0188

1. AGENCY USE ONLY *(Leave blank)*	2. REPORT DATE December 1994	3. REPORT TYPE AND DATES COVERED Master's Thesis

4. TITLE AND SUBTITLE COMPARISON OF SATELLITE-DERIVED MSU BRIGHTNESS TEMPERATURES AND CONVENTIONALLY-DERIVED FIELDS (U)	5. FUNDING NUMBERS
6. AUTHOR(S) Parke, Matthew C.	

7. PERFORMING ORGANIZATION NAME(S) AND ADDRESS(ES) Naval Postgraduate School Monterey CA 93943-5000	8. PERFORMING ORGANIZATION REPORT NUMBER

9. SPONSORING/MONITORING AGENCY NAME(S) AND ADDRESS(ES) National Weather Service, Washington, D.C.	10. SPONSORING/MONITORING AGENCY REPORT NUMBER

11. SUPPLEMENTARY NOTES The views expressed in this thesis are those of the author and do not reflect the official policy or position of the Department of Defense or the U.S. Government.

12a. DISTRIBUTION/AVAILABILITY STATEMENT Approved for public release; distribution is unlimited.	12b. DISTRIBUTION CODE

13. ABSTRACT *(maximum 200 words)*

A statistical analysis is performed on a six-month global data set consisting of satellite-derived channel 3 Microwave Sounding Unit (MSU) brightness-temperatures from the Marshall Space Flight Center and various conventionally-derived fields obtained from the National Meteorological Center Global Data Assimilation System (GDAS) to quantify the potential usefullness of MSU analyses in the nowcasting and forecasting of baroclinic waves especially over data sparse regions. High positive spatial and temporal correlations are obtained between the MSU and the 400-100-mb thickness over all wavelengths in the data. Slightly lesser positive correlations are found between the MSU and the 200-mb temperature. The MSU-500-mb and MSU-50-mb height correlations indicate a scale dependence in the hydrostatic spreading of thickness anomalies in the vertical. Most significantly, relatively high negative MSU-500-mb height correlations for the short ($\leq$ synoptic scale) wave-length portion of the data suggest that upper-level thermal anomalies are reflected downwards and that the MSU can be used to track mid-level synoptic-scale baroclinic waves. This conclusion is also suggested in MSU-500-mb vorticity and MSU-dynamic tropopause correlations. A MSU collection and analysis procedure is also described that demonstrates the practicality and usefulness of generating MSU analyses from locally obtained polar-orbiter data.

14. SUBJECT TERMS Satellite, Microwave Sounding Unit, Tropopause undulations, Forecasting,	15. NUMBER OF PAGES 112
	16. PRICE CODE

17. SECURITY CLASSIFICATION OF REPORT Unclassified	18. SECURITY CLASSIFICATION OF THIS PAGE Unclassified	19. SECURITY CLASSIFICATION OF ABSTRACT Unclassified	20. LIMITATION OF ABSTRACT UL

NSN 7540-01-280-5500

Standard Form 298 (Rev. 2-89)
Prescribed by ANSI Std. 239-18 298-102

Accesion For

NTIS CRA&I	☑
DTIC TAB	☐
Unannounced	☐
Justification	

By _____
Distribution /

Availability Codes

| Dist | Avail and / or Special |

A-1

i

COMPARISON OF SATELLITE-DERIVED MSU BRIGHTNESS TEMPERATURES AND CONVENTIONALLY-DERIVED FIELDS

by

Matthew C. Parke
Lieutenant, United States Navy
B.S., University of South Carolina, 1986

Submitted in partial fulfillment
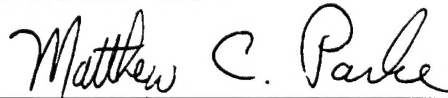of the requirements for the degree of

MASTER OF SCIENCE IN METEOROLOGY AND PHYSICAL OCEANOGRAPHY
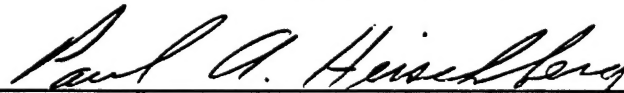
from the

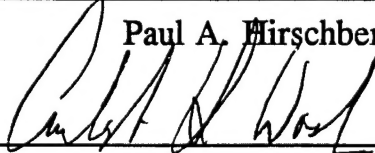## NAVAL POSTGRADUATE SCHOOL
December 1994

Author: _____
Matthew C. Parke

Approved by: _____
Paul A. Hirschberg, Co-Advisor

_____
Carlyle H. Wash, Co-Advisor

_____
Robert L. Haney, Chairman
Department of Meteorology

ABSTRACT

A statistical analysis is performed on a six-month global data set consisting of satellite-derived channel 3 Microwave Sounding Unit (MSU) brightness-temperatures from the Marshall Space Flight Center and various conventionally-derived fields obtained from the National Meteorological Center Global Data Assimilation System (GDAS) to quantify the potential usefullness of MSU analyses in the nowcasting and forecasting of baroclinic waves especially over data sparse regions. High positive spatial and temporal correlations are obtained between the MSU and the 400-100-mb thickness over all wavelengths in the data. Slightly lesser positive correlations are found between the MSU and the 200-mb temperature. The MSU-500-mb and MSU-50-mb height correlations indicate a scale dependence in the hydrostatic spreading of thickness anomalies in the vertical. Most significantly, relatively high negative MSU-500-mb height correlations for the short ($\leq$ synoptic scale) wave-length portion of the data suggest that upper-level thermal anomalies are reflected downwards and that the MSU can be used to track mid-level synoptic-scale baroclinic waves. This conclusion is also suggested in MSU-500-mb vorticity and MSU-dynamic tropopause correlations. A MSU collection and analysis procedure is also described that demonstrates the practicality and usefulness of generating MSU analyses from locally obtained polar-orbiter data.

TABLE OF CONTENTS

ACKNOWLEDGEMENTS

I. INTRODUCTION

The nowcasting and short- and medium-range forecasting of extratropical cyclones and the associated weather patterns that accompany them remains a challenging problem for the operational meteorologist. This is especially true for locations over ocean basins and the western sides of continents. Many upper-level wave and storm systems track from data-sparse regions upstream which limits the accuracy of analyses and numerical simulations of these events. Since their introduction, remotely-sensed satellite products, based on imagery and sounding retrievals, have proven to be invaluable in supplementing general meteorological information over these conventional data-sparse regions.

Currently, the usefulness of satellite data is being further enhanced by the development of products that can provide information about specific processes and features of the atmosphere. For instance, Velden (1992) suggests the potential utility of satellite observations of the upper troposphere and lower stratosphere in locating tropopause-level thermal anomalies. In particular, Velden demonstrates the qualitative applicability of utilizing the 54.96-GHz channel brightness temperature data of the Microwave Sounding Unit (MSU) to infer the position, size, orientation and relative strength of tropopause undulations. These undulations have been shown (Hoskins et al., 1985; Hirschberg and Fritsch, 1991a,b) to be important factors in the structure and evolution of baroclinic waves and cyclones.

In this thesis, a climatological study is presented that quantitatively extends Velden's investigation of the MSU analysis and forecasting tool. Specifically, the utility of the 54.96-Ghz MSU data in locating and forecasting baroclinic waves and cyclones is examined by statistically correlating horizontal analyses and time series of MSU brightness

temperatures to horizontal analyses and time series of various conventionally derived fields over the Northern Hemisphere middle latitudes (25° N to 65° N) during the six-month period 1 October 1993 through 31 March 1994. Ideally, the finding that high correlations exist between the MSU and various conventional fields such as 500-mb geopotential height would enable forecasters to better validate analyses and forecasts over the data-sparse areas at off-synoptic times with a MSU brightness temperature analysis.

II. BACKGROUND

A. DYNAMICAL BACKGROUND

The role of upper-tropospheric/lower-stratospheric features in the structure and evolution of extratropical-baroclinic waves underlies the use of the MSU as a possible nowcasting and forecasting tool. In particular, a recent observational investigation by Hirschberg and Fritsch (1991a,b) have demonstrated that tropopause-level temperature anomalies and temperature advections are important in the hydrostatic structure and development of extratropical cyclones. Numerical and analytical model studies by Jusem and Atlas (1991), Hirschberg and Fritsch (1993a, 1994), and Hirschberg and Doyle (1994) compliment this observational study. Furthermore, the development of "IPV thinking" concepts by Hoskins et al., (1985) provide a rigorous theoretical foundation for the importance of tropopause-level dynamics during cyclogenesis. Studies focusing on PV and its role in cyclogenesis are increasing in the literature (e.g. Hoskins et al., 1985; Hoskins and Berrisford, 1988; Davis and Emanuel, 1991; Bell and Bosart, 1993).

1. Hydrostatic Balance and Geopotential Height Tendency

Within the traditional quasi-geostrophic framework, two diagnostic tendency equations are useful in understanding the different roles that vorticity and thermal structure play in the initiation, intensification, and demise of surface cyclones. These are the geopotential height tendency equation and the omega equation which form a closed set of equations in Φ and ω (Holton, 1979).

3

The quasi-geostrophic height tendency equation is

$$(\nabla^2+\frac{f_0^2}{\sigma})\chi=-f_0 \mathbf{v}_g \cdot \nabla(\frac{1}{f_0}\nabla^2\Phi+f)+\frac{f_0^2}{\sigma}\frac{\partial}{\partial p}(-\mathbf{v}_g \cdot \nabla\frac{\partial\Phi}{\partial p}), \qquad (1)$$

where $\chi=\partial\Phi/\partial t$, f_0 is a constant Coriolis parameter, f is the latitudinal varying Coriolis parameter, $\mathbf{v}_g$ is the horizontal geostrophic wind, σ is the static stability parameter, and Φ is the geopotential height. The term on the left side (LS) is a Laplacian operator which tends to make χ negative when the right side (RS) of equation (1) is positive. It represents the increase/decrease of height for a negative/positive (RS). The first term on the (RS) of equation (1) represents the effects of advection of absolute vorticity while the second term on the (RS) represents the effects of differential thickness advection and can be considered to be a measure of the advection of temperature (Holton, 1979). Equation (1) states that for height falls to occur on an arbitrary pressure surface there must be either positive advection of absolute vorticity (PVA) or differential cold air advection (CAA). Of course, a combination of both effects in varying degrees can still produce height falls as long as the effects combine with a residual positive effect.

Holton (1979) presents the omega equation as

$$(\nabla^2+\frac{f_0^2}{\sigma}\frac{\partial^2}{\partial p^2})\omega=\frac{f_0}{\sigma}\frac{\partial}{\partial p}[\mathbf{v}_g \cdot \nabla(\frac{1}{f_0}\nabla^2\Phi+f)]+\frac{1}{\sigma}\nabla^2[\mathbf{v}_g \cdot \nabla(-\frac{\partial\Phi}{\partial p})], \qquad (2)$$

where the variables are the same as equation (1) with the exception of ω, which is the vertical velocity. The omega equation shows that vertical velocity is a function of differential vorticity advection and thickness advection. In the case of cyclogenesis, there is generally a large area of rising air ahead of a surface low with sinking air behind.

4

This is in response to the geostrophic forcing and ensures that thermal wind balance is maintained.

Conventional expositions (Holton, 1979) of quasi-geostrophic extratropical cyclogenesis hold that height falls at 500 mb in a developing baroclinic wave can be produced by either PVA or CAA (Fig. 1). These dynamical processes in a simplified sense operate at different locations along the wave. PVA between the upper-level trough axis and the downstream ridge tends to decrease the heights through divergent mass export. Meanwhile, CAA in the 1000 - 500 mb layer behind the surface cyclone and underneath the 500-mb trough causes the thickness of the layer to decrease with a hydrostatic lowering of the 500 mb surface. Implicit in the last statement, however, is the assumption of a fixed lower boundary (1000 mb). This forces the effects of the temperature advection to be reflected at the upper pressure level, in this case at 500 mb. Partially, as a consequence of this conceptualization, cyclogenesis has traditionally been viewed to be forced primarily in the mid- to- lower troposphere. In addition, temperature advection has been thought to be largest at low- to- mid levels and to diminish in importance above 500 mb.

On the contrary, cross sections through developing baroclinic waves (Fig. 2) often show synoptic-scale undulations along the tropopause. Characteristically, these undulations have half wavelengths between 1500 - 2000 km and vertical amplitudes of over 200 mb. Where the tropopause is more steeply inclined, it separates adjacent pools of relatively warm stratospheric air (above the low portion of the undulation) from relatively cooler tropospheric air (below the high portion of the undulation). These adjacent pools represent warm/cold temperature deviations, or anomalies with respect to the background environmental temperature. In addition, these anomalies are almost perpendicular to the flow

5
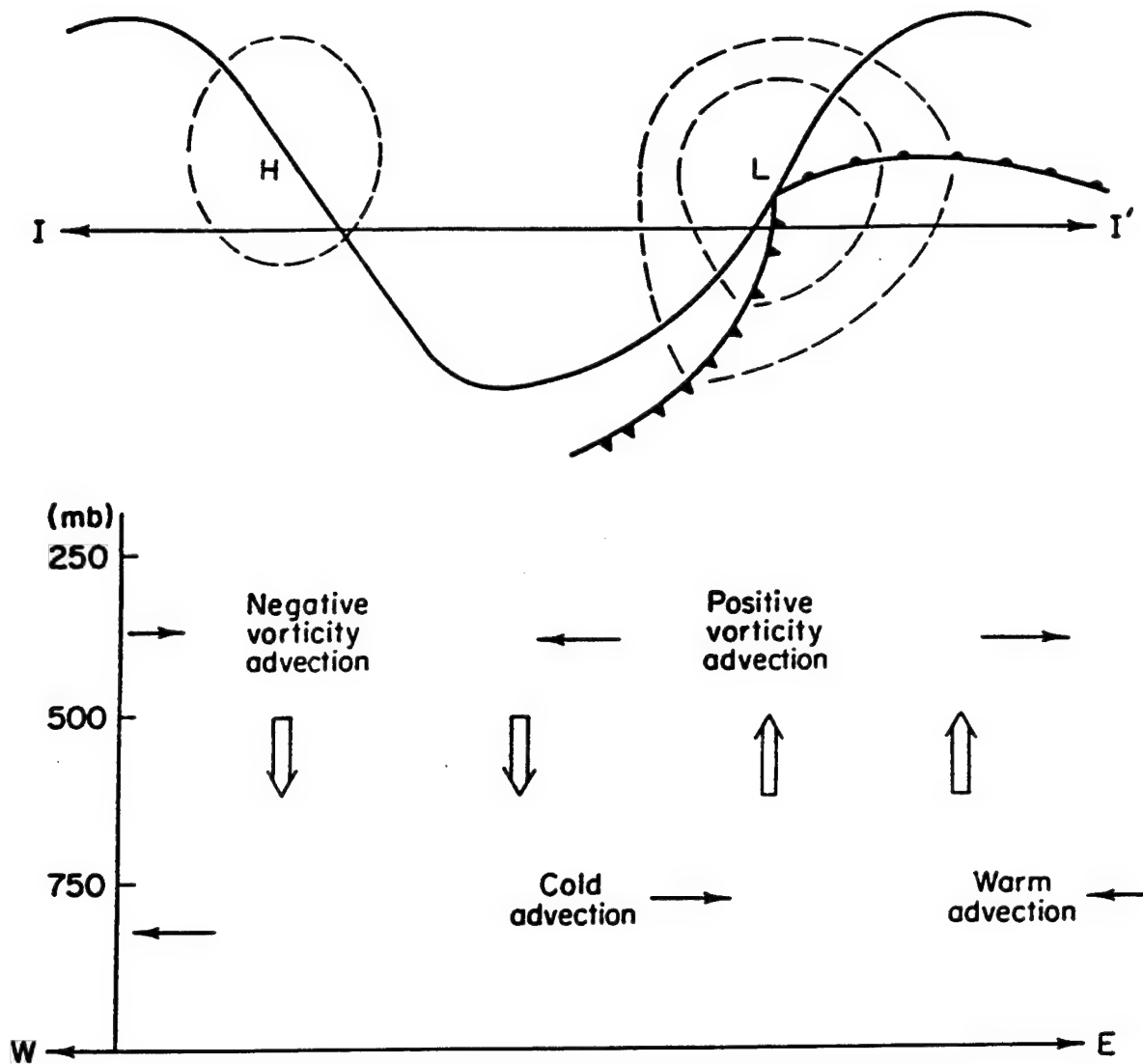
Figure 1. Secondary circulation associated with a developing baroclinic wave:
(top) schematic 500-mb contour (solid line), 1000-mb contours (dashed lines),
and surface fronts; (bottom) vertical profile through the line II' indicating
the divergent and vertical motion fields. From Holton (1979).
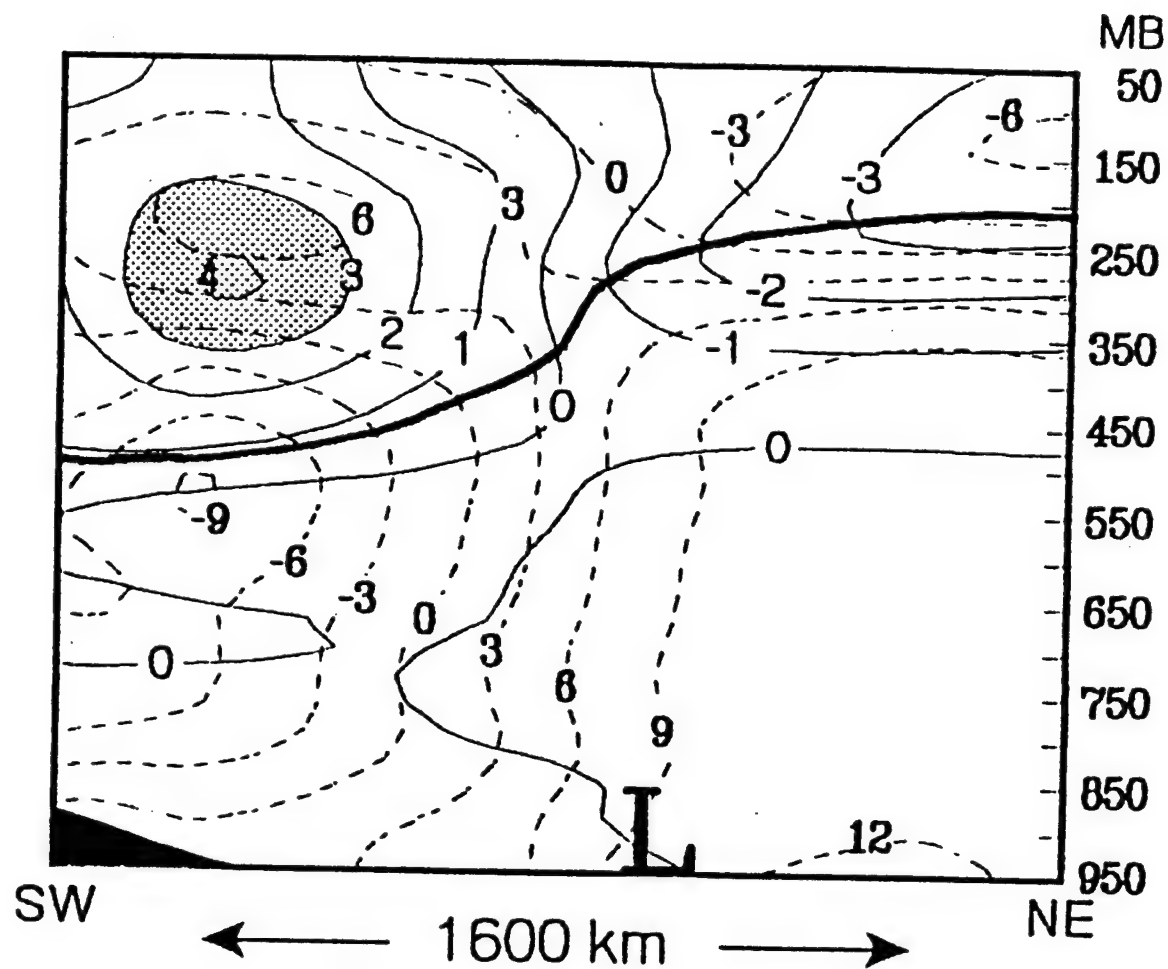
Figure 2. Southwest to northeast cross section of observed perturbation isentropic PV (solid, 10^{-6} m^2 s^{-1} K kg^{-1}) and perturbation temperature (dashed, K). Stippling denotes regions with anomalously high values of PV. The dynamic tropopause (PV value of [1.0×10^{-6} m^2 s^{-1} K kg^{-1}]) is denoted by a heavy solid line and the position of the surface low by an "L". From Hirschberg and Fritsch (1991a).

during developing situations. Therefore, the potential for large temperature advections exist within the upper troposphere/lower stratosphere.

Hirschberg and Fritsch (1991 a,b), drawing on the results of much earlier studies (Godson, 1948), discuss the implications of observed strong temperature advection in the upper troposphere along the tropopause during cyclogenesis. In particular, they examine the effects of upper-level temperature tendency by analyzing an alternative height tendency equation formed by taking the temporal derivative of the hypsometric equation,

$$\frac{\partial z(p_t)}{\partial t} - \frac{\partial z(p_b)}{\partial t} = -\frac{R}{g}\int_{P_b}^{P_t} \frac{\partial T_v}{\partial t}\, dlnp. \qquad (3)$$

By substituting the inviscid form of the 1st Law of Thermodynamics for $(\partial T_v/\partial t)$ and assuming diabatic effects are encompassed by pseudo-adiabatic latent heat release on the synoptic-scale, they find that the instantaneous geopotential height tendency at a lower pressure level is given by

$$\frac{\partial z(p_b)}{\partial t} = Z_t(p_b) = \frac{R}{g}\int_{P_b}^{P_t} (-\mathbf{v}.\nabla T_v + \omega S_a)\, dlnp + \frac{\partial z(p_t)}{\partial t}, \qquad (4)$$

where $Z_t(p_b)$ is the instantaneous height tendency at the arbitrary lower pressure level, T_v is the virtual temperature, ω is the vertical velocity, and S_a is a common parameterization scheme for static stability that includes both vertical velocity and moisture effects (see Hirschberg and Fritsch, 1991b for details). If a "level of insignificant dynamics" (LID) is assumed at the top level (P_t), then the instantaneous height tendency at this level $(\partial z(p_t)/\partial t)$ is approximately zero. Hirschberg and Fritsch (1991a) argue that a LID assumption is valid in a highly stable, low ambient density environment. These requirements are found to be met

8

within the upper levels of the stratosphere. Significantly, owing to its logarithmic dependence, equation (4) shows that upper-level temperature advection not completely offset by vertical motion can drive low-level height changes in the presence of a LID.

Based on their analysis, Hirschberg and Fritsch conceptualize (Fig. 3) that tropopause-level temperature anomalies are important in the hydrostatic structure of mid- to- lower troposphere baroclinic waves and that the associated upper-level temperature advections can influence the development of these waves. In particular, troughs (ridges) can be hydrostatically induced below tropopause-level warm (cold) anomalies. Furthermore, these warm/cold anomalies that occur along the tropopause are often associated with positive/negative potential vorticity (PV) anomalies. In particular, note the association of high perturbation PV with warm departures of temperature (Fig. 2).

2. Potential Vorticity Considerations

An important quantity in the understanding of cyclogenesis is potential vorticity. The theoretical foundation for potential vorticity dynamics was first developed by Rossby (1940) and Ertel (1942), but its full application was diminished by the development of quasi-geostrophic theory. Recently, Hoskins et al., (1985) provided the impetus for the resurgence in popularity of potential vorticity concepts with their paper emphasizing "IPV thinking."
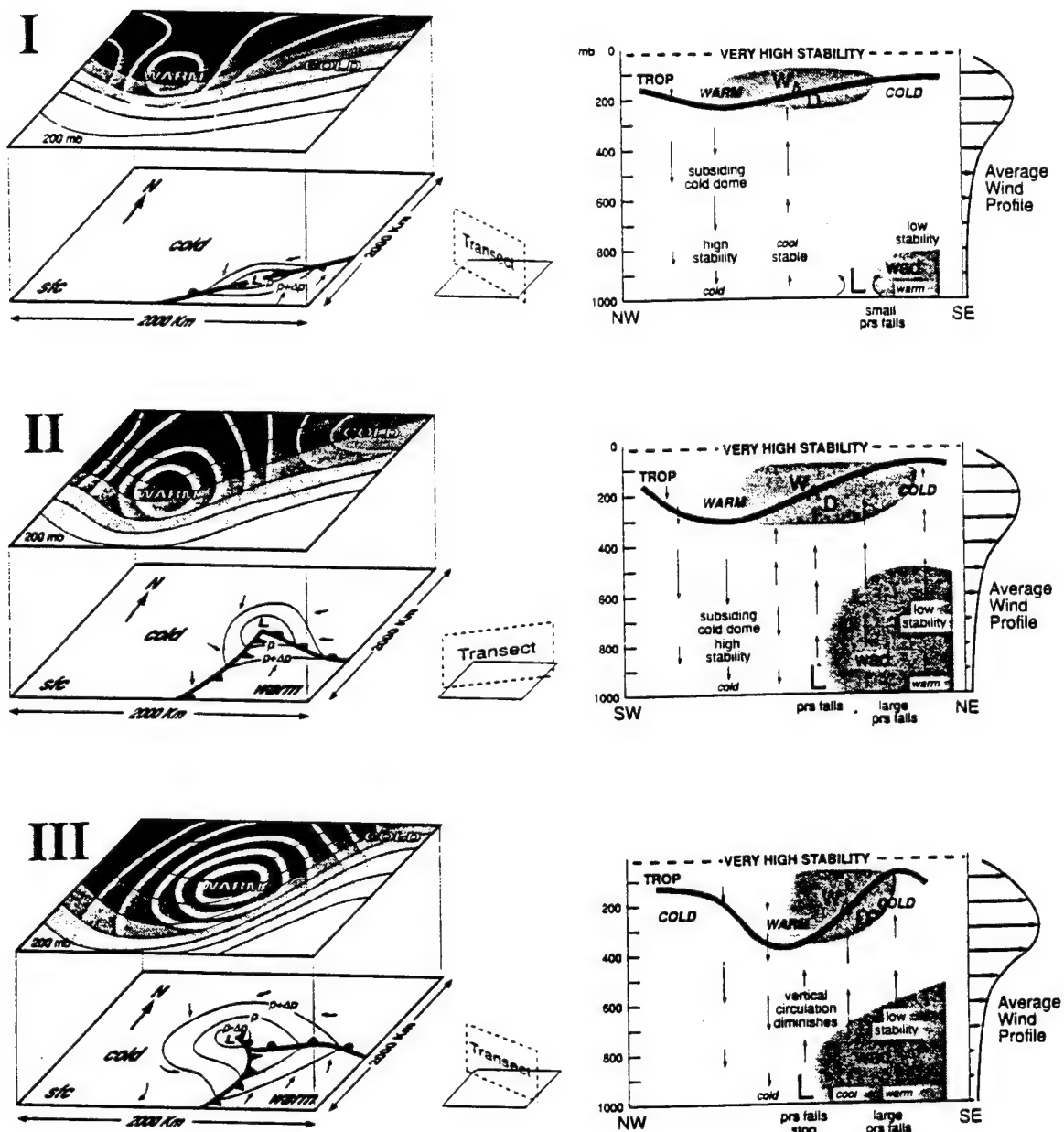
Figure 3. Schematic diagrams illustrating Hirschberg and Fritsch's (1991b) conceptual model of the development and evolution of an extratropical cyclone. Diagrams on the left depict a three-dimensional view of the configuration of the 200-mb heights (solid black lines and shading) and temperatures (solid white lines) as well as the surface low and surface pressures (thin solid black lines). Arrows denote horizontal flow around the surface low. Surface fronts and the relative temperature structure are also shown. The diagrams on the far right depict cross sections along transects shown adjacent to the surface representations. The relative positions of the tropopause (heavy solid line), surface low (L), vertical motion (arrows), warm advection (WAD - stippled), and average wind profile are depicted in the cross sections as well as the relative temperature, pressure change, and static stability regimes. I. Out-of-phase stage: The temperature anomalies associated with a tropopause undulation approach a shallow surface low. II. Developing stage: The strongest upper-level warm advection associated with the tropopause undulation is directly over the surface low. III. Occluded stage: The surface low is directly underneath the warm pool in the lower stratosphere and the low portion of the tropopause undulation. From Hirschberg and Fritsch (1991b).

10

Potential vorticity in a quasi-geostrophic (QG) framework is captured in the QG potential vorticity equation in isobaric coordinates

$$\frac{dq}{dt} = \frac{\partial q}{\partial t} + v_g \cdot \nabla_p q = 0, \tag{5}$$

where

$$q = \frac{\nabla^2 \phi}{f_0} + f + \frac{f_0}{\sigma} \frac{\partial^2 \phi}{\partial p^2}. \tag{6}$$

In (6), q is the geostrophic potential vorticity, v_g is the horizontal geostrophic wind, ϕ is the geopotential, f_0 is a constant coriolis parameter, f is the latitudinally-varying coriolis term, and σ is the static stability parameter and is assumed constant. The first term on the right side of equation (5) represents the geostrophic relative vorticity, the second term the planetary vorticity, with the last term representing the effects of vertical stretching/shrinking of a vortex tube.

The QG potential vorticity equation (5) encompasses both dynamic (wind, vorticity) and thermodynamic (mass, temperature) information. This "encapsulation" of several parameters (v, ω, T, p) into PV simplifies the understanding of baroclinic flow dynamics. QG potential vorticity (q) is conserved following the motion on isobaric surfaces provided the flow is frictionless and adiabatic. This is approximately true in the real atmosphere for a period of several days provided vertical advection and diabatic processes such as latent heat release from condensation is negligible (Hoskins and Berrisford, 1988). Since (5) represents the QG form of the potential vorticity equation, it is more appropriate to refer to it as the "pseudopotential" vorticity equation, a phrase coined by Charney and Stern (Hoskins et al., 1985).

11

Ertel's (1942) form of potential vorticity is

$$P = \frac{1}{\rho} \zeta_a . \nabla\theta = constant. \tag{7}$$

The significance of P is that it is conserved for adiabatic, frictionless motion, and since there are no assumptions made as in the QG approximations, it covers a wider class of flow regimes. Typically, the hydrostatic isentropic form of the potential vorticity, given by

$$P_\theta = -g(\zeta_\theta + f) \frac{\partial\theta}{\partial p} \tag{8}$$

is used to study atmospheric dynamics. In equation (8) P_θ is the potential vorticity on an isentropic surface, that is, a surface in which the potential temperature (θ) is conserved, and (ζ_θ + f) is the vertical component of the absolute vorticity on an isentropic surface. Importantly, equation (8) contains dynamical (ζ_θ + f) and temperature ($\partial\theta/\partial p$) information.

Climatologically large values of potential vorticity are found in the stratosphere owing primarily to large static stability thought to result from a combination of diabatic heating of ozone plus diabatic cooling (longwave radiation) within the troposphere. Hoskins et al. (1985) state that PV increases from (0.5 PV units) (1 PV unit = 10^{-6} $m^2 s^{-1}$ K kg^{-1}) in the troposphere to 4 units in the stratopsphere. Accordingly, many researchers define the tropopause in terms of a "dynamic tropopause" identified as the 2 PV unit surface of the tropopause. This definition contains both dynamic and thermodynamic information in contrast to the current World Meteorological Organization (WMO) definition and should provide a more objective means for locating the tropopause as illustrated in (Fig. 4).

12
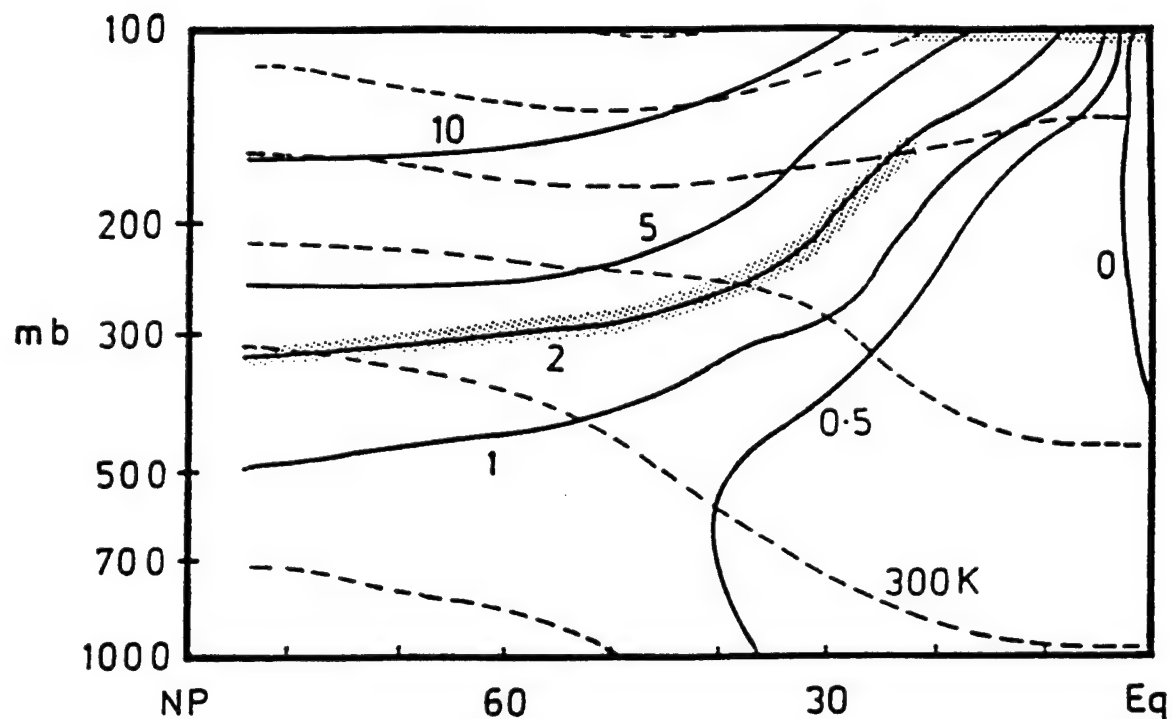
Figure 4. North to South climatological cross section indicating the winter distribution of potential vorticity (PV) below 100 mb. Dashed contours are potential temperature (θ) drawn every 30 K. PV contours (heavy solid lines) are labelled as 0, 0.5, 1, 2, 5, and 10 PVU where 1 PVU = 10^{-6} K m² kg⁻¹ s⁻¹. The "dynamic" tropopause, specified by 2 PVU, is indicated by stippling. From Hoskins et al. (1985).

13

The role of PV anomalies in cyclogenesis has become clear since the publication of Hoskins et al. (1985). A PV anomaly is a deviation of the PV distribution from the background ambient distribution of PV. Positive PV anomalies have values larger than the mean PV distribution, while negative PV anomalies are less than the mean. Large upper-level PV anomalies are typically associated with undulations along the tropopause with positive anomalies generally found near low portions of tropopause undulations (stratospheric origin) and negative anomalies near high portions (tropospheric origin). Consequently, positive PV anomalies at the tropopause level are associated with the warm temperature anomalies above them that Hirschberg and Fritsch (1991b) concentrate on. The warm anomalies result from the gradual sinking of stratospheric air, which, because of the high static stability typical in this region, needs only small values of downward motion to produce correspondingly large temperature increases (Carlson, 1991).

The evolution of these upper-level thermal and PV features and PV are related to the evolution of 3-d baroclinic waves and surface cyclones. Most significantly, PV anomalies induce circulation changes in the surrounding environment and both observational (Bleck et al., 1984; Hoskins et al., 1985) and numerical (Bleck, 1973; Bleck, 1974) studies have concluded that the superposition of an upper-level positive PV anomaly with a low-level baroclinic zone is conducive to cyclogenesis (Fig. 5).

In another context, since isentropic potential vorticity (IPV) is generally conserved, absolute vorticity must increase following parcel motions if that motion is towards an environment of decreased static stability. That is, if

14
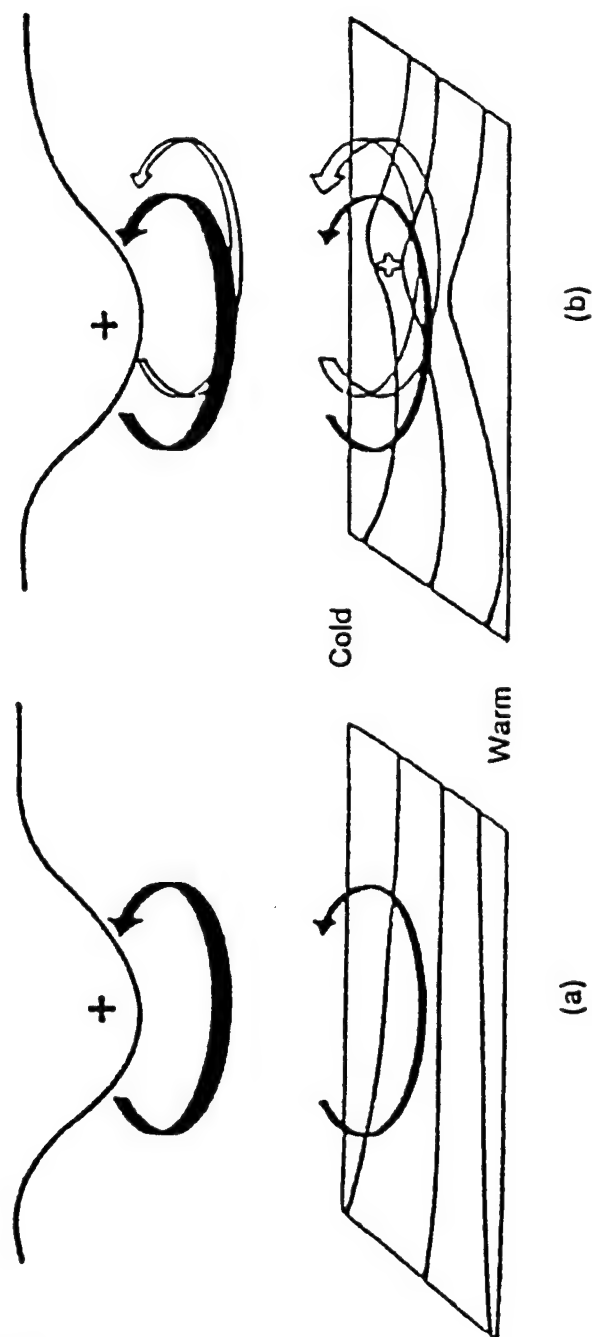
Figure 5. A schematic picture of cyclogenesis associated with the arrival of an upper-level PV anomaly over a low-level baroclinic region. In (a) the upper-air cyclonic PV anomaly (solid plus sign) is associated with a low tropopause and has just arrived over a region of significant low-level baroclinicity. The circulation of the upper-level PV anomaly (thick dark arrow) induces a low-level circulation (thin black arrow) over the θ field at the surface. The advection of this circulation leads to a warm anomaly ahead of the upper PV anomaly indicated in (b) as an open plus sign. This warm anomaly induces a cyclonic circulation (open arrows in (b)). The upper-level PV anomaly is reinforced by the surface induced upper-level circulation (thin open arrow in (b)) if there is advection of high PV (lower stratosphere) air equatorward and poleward advection of low PV of upper-tropospheric origin. From Hoskins et al. (1985).

15

$$\frac{d}{dt}(\zeta_{\theta_e}) > 0,$$

(9)

then a corresponding increase in the absolute vorticity,

$$\frac{d}{dt}\left(-\frac{\partial\theta}{\partial p}\right) < 0,$$

(10)

must occur. One situation where this occurs is when high static stability air associated with the stratosphere is advected into the reduced static stability environment of the troposphere. Indeed, this is one theory for the generation of mid- to- low level vorticity needed for cyclogenesis, especially in rapidly developing cyclones (Uccellini et al., 1985). In these instances (Fig. 6), high PV air of stratospheric origin is advected down isentropic surfaces in so-called "tropopause folds" or upper-level fronts as described by Keyser and Shapiro (1986). Although it has not been completely resolved to what extent tropopause folding is necessary for cyclogenesis to occur, it certainly serves to focus and intensify the process.

To summarize, studies over the last 20 years have shown the upper tropophere/lower stratosphere to be areas of strong dynamical forcing during extratropical cyclogenesis. This forcing is now thought to be important in cyclogenesis. Consequently, proper identification of features such as tropopause-level thermal and PV anomalies will aid in the analysis and forecasts of these events. Fortunately, these features can be sampled or derived with conventional data. However, the conventional observation network is not perfect and large areas exist over the globe that are poorly observed. As such, a device that can provide additional information and whose output is closely linked with these upper-level features would greatly aid a forecaster. Remotely-sensed satellite data can potentially fill this need.

16
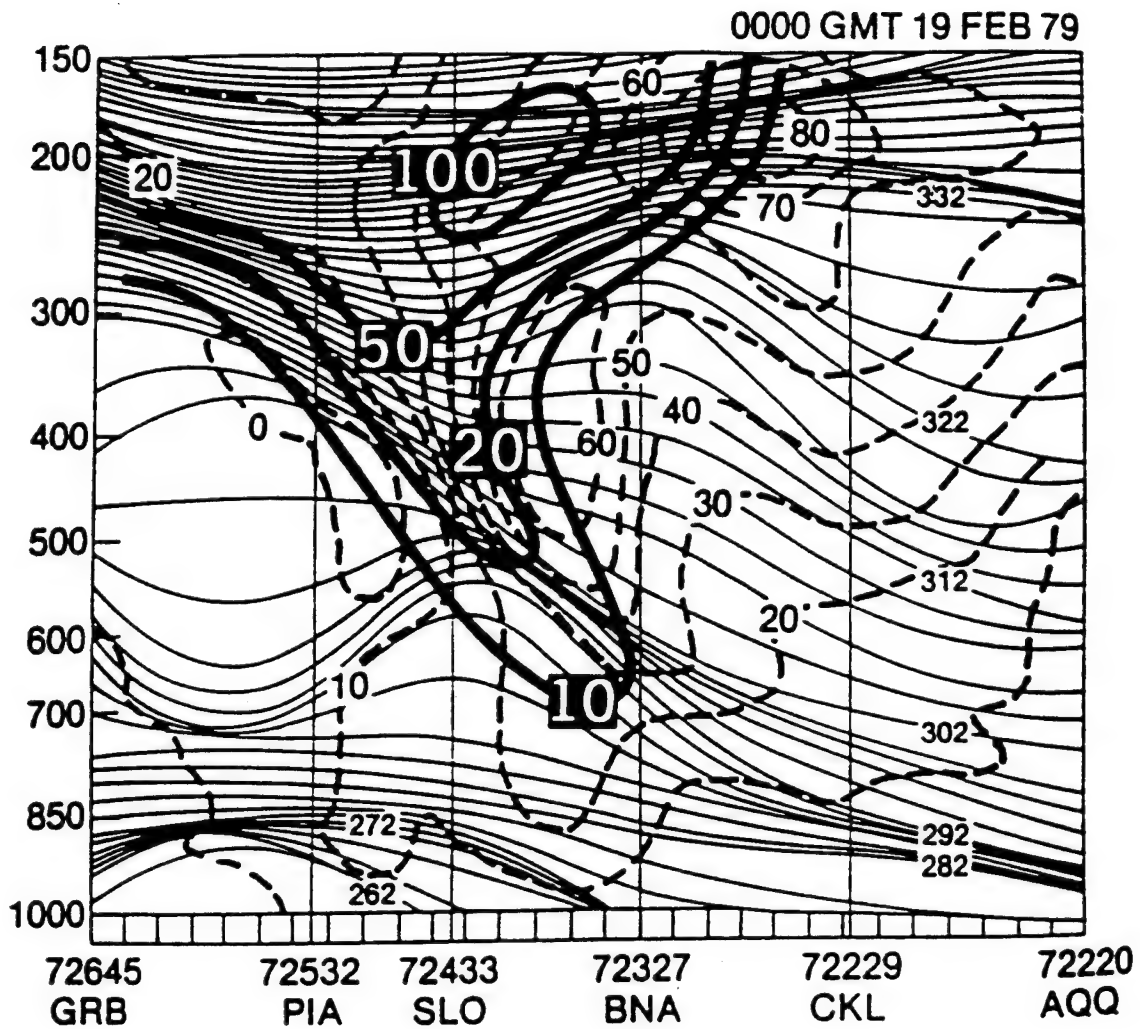
Figure 6. Vertical cross section from Green Bay, Wisconsin (GRB) to Appalachicola, Florida (AQQ) for 0000 UTC 19 February 1979 indicating the development of an upper-level front (tropopause fold). Isentropes (solid, K), geostrophic wind (dashed, m s^{-1}), and potential vorticity (heavy solid) 10^{-6} K mb^{-1}. From Uccellini et al., (1985).

17

B. REMOTE SENSING CONCEPTS

The use of remote sensors to monitor the atmosphere has evolved over the last 30 years. Initially, low-resolution photographs of the surface of the earth and large-scale cloud structure in the atmosphere were the only information provided, but as time progressed more sophisticated methods for monitoring the temperature structure, moisture content, and gaseous composition of the atmosphere were developed. Development of new sensors were based on the radiation characteristics of the atmosphere. These physical processes are embodied in the radiative transfer equation (Kidder and Vonder Haar, 1994)

$$\frac{dL_\lambda}{ds} = -\sigma_a(\lambda) L_\lambda(\theta,\phi) - L_\lambda(\theta,\phi) + \sigma_a(\lambda) B_\lambda(T) \\ + \frac{\sigma_s}{4\pi} \int_0^{2\pi} \int_0^{\pi} L_\lambda(\theta',\phi') p(\psi_s) \sin(\theta) \, d\theta' d\phi, \tag{11}$$

where the term on the left is a measure of the rate of change of radiance for an arbitrary path. The first term on the right represents the absorption of radiation by the intervening medium, the second term is a measure of the scatter of radiation out of the volume, the third term represents the emission of radiation by particles or molecules within the volume, and the fourth term accounts for radiation scattered into the volume from any arbitrary direction.

At microwave frequencies scattering effects are negligible (Kidder and Vonder Haar, 1994). Therefore, the scattering terms in the radiative transfer equation can be dropped. A further simplification results from the linear relationship between the brightness temperature (T_b) and

18

temperature at a particular pressure level (T_p). This simplification occurs through use of the Rayleigh-Jeans approximation of the Planck function

$$B_\lambda(T) = \frac{2hc^2\lambda^5}{\exp(\frac{hc}{\lambda kT}) - 1},$$ (12)

where $B_\lambda(T)$ is the blackbody radiance of the body, λ is the wavelength, c is the speed of light in a vacuum, k is Boltzmann's constant, T is the temperature of the body, and h is the Planck constant. At the relatively long wavelengths in the microwave region, $hc/\lambda kT \ll 1$ and $\exp(hc/\lambda kT)$ can be approximated as $1 + hc/\lambda kT$ with the Planck function simplifying to

$$B_\lambda(T) = \frac{c_1}{c_2}\lambda^{-4}T,$$ (13)

where $c_1 = 2hc^2$ and $c_2 = hc/k$. Equation (13) indicates that the blackbody temperature is directly related to the temperature of the body at millimeter and centimeter wavelengths and in the microwave region it is customary to divide the radiance values by $(c_1/c_2)\lambda^4$ and refer to the resulting temperature value as the brightness temperature (Kidder and Vonder Haar, 1994).

Molecular oxygen (O_2) is a well-mixed gas in the atmosphere and is considered constant both in space and in time (Machta and Hughes, 1970). Utilizing the absorption and re-emission characteristics of molecular oxygen, pressure and temperature as a function of height can be determined for discrete pressure levels of the atmosphere (Meeks and Lilley, 1963). In the microwave region, molecular oxygen has an absorption region between 50 Ghz and 70 Ghz that peaks around 60 Ghz. Because of its well-mixed distribution and its monotonic decrease of concentration with increasing altitude,

19

stronger absorption of radiation by O_2 equates to higher
levels of the atmosphere. Therefore, by making observations
on the edges of the O_2 "absorption band," the determination of
brightness temperature (T_b) as a function of height is
realized.

Transfer of electromagnetic radiation leading to T_b at
microwave frequencies is attributable to 3 sources. These
include "direct" upwelled radiance by the atmosphere,
"indirect" or reflected atmospheric radiation from the
surface, and surface emission upwelled through the mostly
opaque atmosphere (Spencer et al., 1990).

Following the development by Spencer et al., (1990),
brightness temperature as measured by an orbiting satellite is
given by

$$T_b(\upsilon) = \int_{\ln p_s}^{-\infty} T_p \left[\frac{d\tau_\upsilon(p)}{d\ln p} \right] d\ln p + \tau_\upsilon(p_s) T_s, \qquad (14)$$

where T_b is the brightness temperature, υ is the frequency, τ
is the transmittance, p_s is the surface pressure, p is the
pressure at a particular height, and T_s is the surface skin
temperature. The effective transmittance (τ_υ) is a
combination of many familiar parameters of the radiative
transfer equation and is given by

$$\overline{\tau}_\upsilon(p) = \left[1 - (1 - e_s(\upsilon, \theta)) \frac{\tau_\upsilon(p_s)}{\tau_\upsilon(p)^{2\sec\theta}} \right] \tau_\upsilon(p)^{\sec\theta}, \qquad (15)$$

where e_s is the surface emissivity and is a function of both
frequency and earth incidence angle (θ). The atmospheric
absorption term $\tau_\upsilon(p)$ represents the exponential absorption
along the vertical path between the satellite and an arbitrary
pressure level. The $(1-e_s)$ term represents the reflectance

from the surface of the earth. The effective transmittance, that is, the emittance by the volume of atmosphere being sampled is given by

$$\overline{\tau}_v(p_s) = \tau_s(p_s)^{\sec\theta} e_s. \tag{16}$$

The increased absorption due to the longer path lengths as the satellite scans off nadir is accounted for in the sec θ term. Therefore, $T_b(v)$ represents a pressure-weighted atmospheric brightness temperature that is dependent on the weighting function $-(d\tau_v(p)/d\ln p)$ (Fig. 7). In the case of a well-mixed atmospheric gas, the weighting function has a maximum value that tails off both above and below the maximum in accordance with the transmittance strength of the substance as the frequency is varied. In Figure 7 note the rise in the weighting function as the scan edge is reached.

These weighting functions are empirically derived and are well described for well-mixed gases. Although it is typical to take MSU data and invert it through equation (14) to arrive at a temperature profile of the atmosphere, it is also possible to consider the MSU values for what they are - that is, a representation of a vertically-averaged temperature measurement of the atmosphere (Spencer et al., 1990). However, to accurately represent the weighted function, it must have a unique pressure dependence structure for a given frequency. This means that the absorption of radiation at a particular frequency must be dominated by the well-mixed gas whose absorption increases uniformly with pressure, the absorption due to variable constituents such as water vapor and clouds must be very small compared to the uniformly mixed gas, and the surface emissivity variations must be small compared to the brightness temperature changes due to atmospheric temperature. The above requirements are met by

21
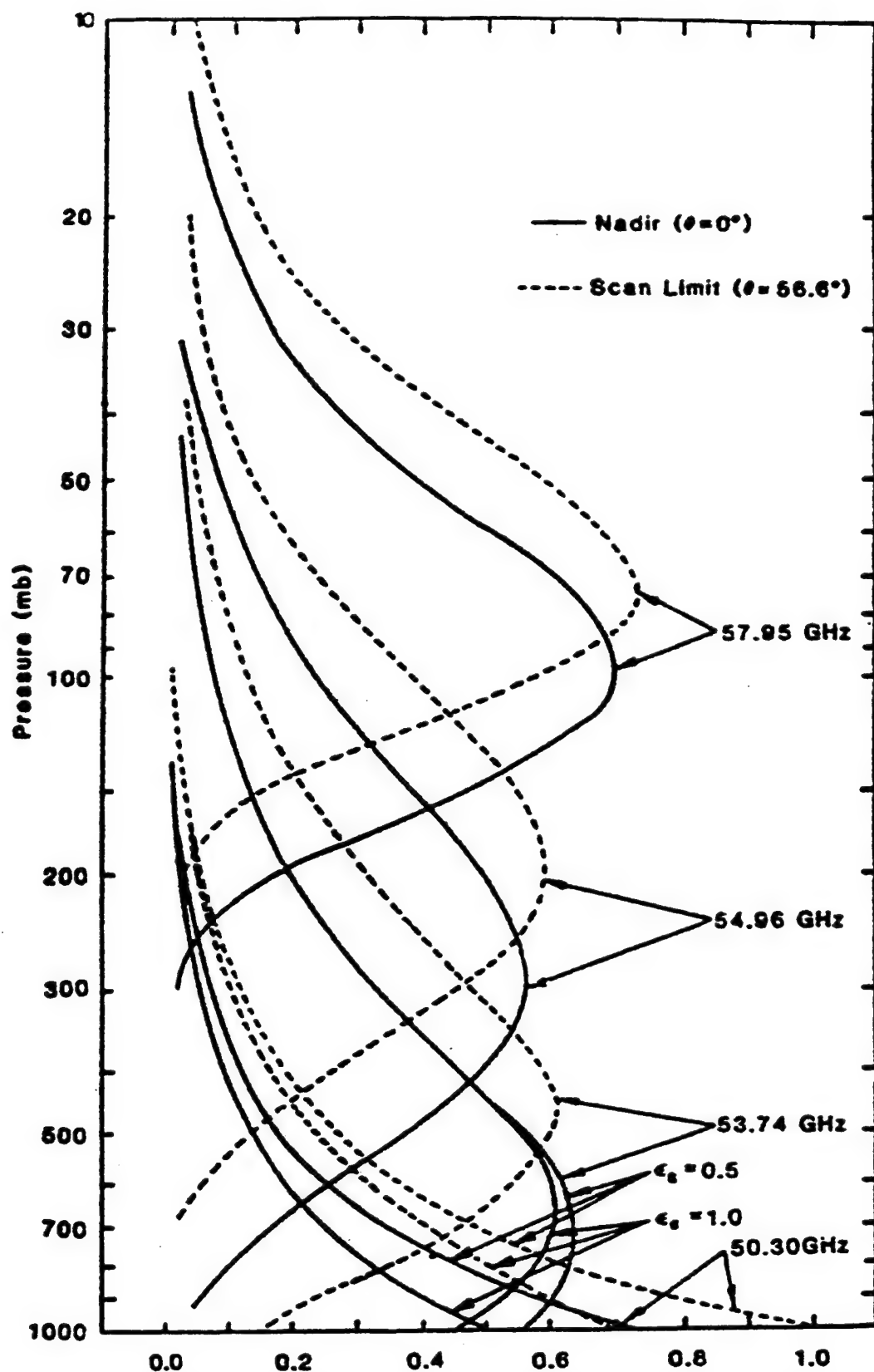
Figure 7. MSU weighting functions calculated from nadir and scan limit positions. From Grody (1983).

22

the highest 3 channels of the MSU (Spencer et al., 1990). As will be discussed later, to exclude precipitation effects on the microwave signal (as well as for other reasons), channel 3 MSU data were chosen as the focal point of this study.

C. THE MICROWAVE SOUNDING UNIT

The Microwave Sounding Unit (MSU) is flown aboard the TIROS-N series of polar orbiting satellites operated by the National Oceanic and Atmospheric Organization (NOAA). The MSU consists of a four-channel passive microwave system that contains four individual Dicke-type radiometers that measure the thermal emission in the oxygen absorption region (Table 1).

MSU Channel	Frequency (GHz)
1	50.30
2	53.74
3	54.96
4	57.95

Table 1. MSU Channel versus Frequency (GHz). The center of the O_2 absorption band is near 60 GHz.

The system encompasses a pair of scanning reflector antennas that directs incoming radiation into a corresponding pair of circular horn antennas. These horn antennas distribute the incoming radiation to the radiometers (Grody, 1983). The 7.5° beamwidth of the system is set by the physical dimensions of the reflector antennas and result in an ~3 dB, or half-power footprint at nadir of about 110 km for a satellite operating near 830 km altitude (Fig. 8). Thus, only

23
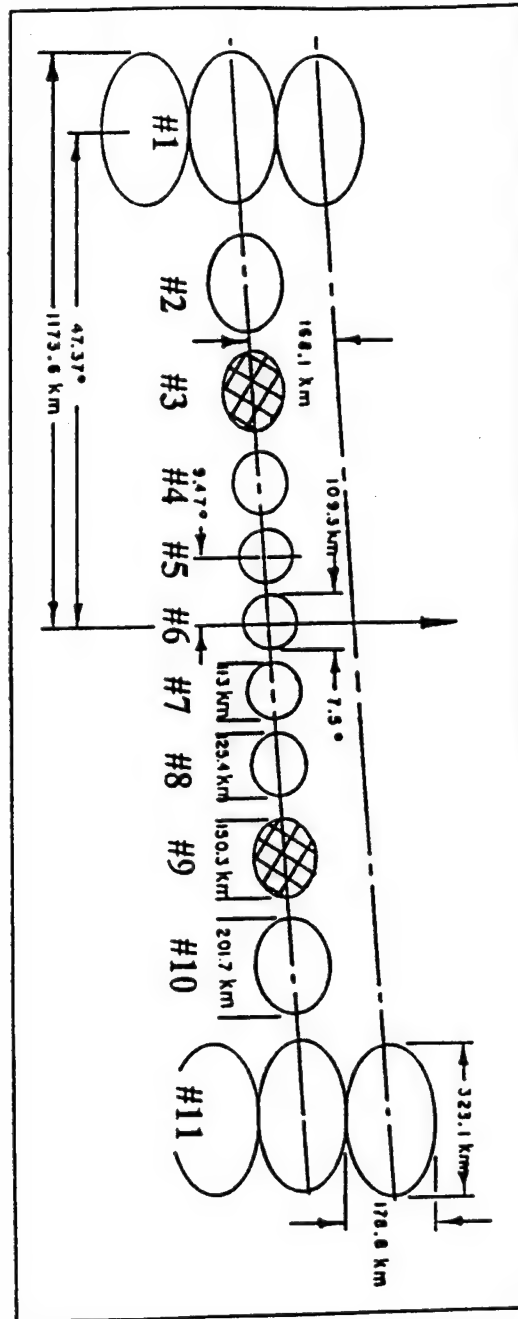
Figure 8. MSU scan grid pattern and field of view (half-power) projected on Earth. The scan positions are labelled as #1, #2 and so on. Scan positions #3 and #9 are utilized in the "intermediate" or non-nadir limb correction technique. The long thin arrow through nadir (footprint #6) gives the direction of spacecraft flight. From Spencer et al. (1994).

24

a small amount of radiation (2-4%) is received from outside the main lobe (Spencer et al., 1990).

The incoming microwave energy is separated into vertical and horizontal components with each of the four resulting signals being fed to one of the radiometer channels. A two-point calibration of the radiometers is accomplished once per scan. This process involves alternately looking at cold space and a stable blackbody (Rao et al., 1990). The calibration of the MSU each scan means that each scan line is independent of other scans (Spencer et al., 1990).

As can be seen in Figure 8, the MSU samples 11 instantaneous fields of view (IFOV) within its cross-track swath. A sample is processed on average every 0.4 s (Spencer et al., 1990). As the system scans away from nadir, the footprint becomes more elliptical and reaches its maximum areal extent at the edge of the swath. Due to the longer path length encountered toward the swath edges there is an apparent rise in the weighting functions of about 30% (Fig. 7) that results in the MSU channels becoming more cold biased toward the swath edges (Grody, 1983). This apparent rise in the weighting functions is known as "limb darkening" and must be accounted for. There are several means for limb correcting the MSU data and these will be discussed in Chapter III.

D. VELDEN'S QUALITATIVE APPLICATION

The radiance measurements from channel 3 (54.96 GHz) of the MSU represent a layer-average (400 - 100 mb) brightness temperature owing to the weighting function characteristics of the channel (Fig. 7). Consequently, horizontal analyses of these brightness temperatures may serve as an aid in locating and tracking tropopause-level thermal anomalies that have been shown to be intrinsic in the structure and evolution of baroclinic waves. Furthermore, minimal attenuation of the channel 3 signal from cloud and ice precipitation enables

successful utilization of the information obtained from this channel even in extensively cloudy conditions when other sensors such as the High Resolution Infrared Sensor (HIRS) may fail (Velden, 1992).

Velden (1992) qualitatively demonstrated the ability of the channel 3 MSU to detect and track upper-level thermal anomalies by comparing the channel 3 MSU brightness temperature analyses to the various isobaric temperature and sea-level pressure analyses during four cases of cyclogenesis. Two of these cases involved a prolonged rapid deepening phase, one was evidenced by a slow deepening phase followed by a shorter rapid deepening phase, and the final case was characterized by non-development. Two of the events were selected at random from NOAA satellite passes that were collected in real-time at the University of Wisconsin (an explosive deepener and a non-explosive deepener). The other two cases occurred during the Experiment on Rapidly Intensifying Cyclone over the Atlantic (ERICA).

In all four cases, Velden found warm anomalies in the channel 3 MSU patterns that corresponded to the low portions of the tropopause undulations as described by Hirschberg and Fritsch (1991a,b). These channel 3 MSU warm anomalies best matched the 250-mb thermal anomalies during these events. In agreement with the Hirschberg and Fritsch (1991b) conceptual model, Velden found that the warmest channel 3 MSU brightness temperature "pixels" were generally located southwest of the surface low center during development. Furthermore, he found that this brightness temperature anomaly intensified as the surface low deepened until the upper-level "warm pool" became collocated with the low. At this point, the system became occluded and no further deepening took place. Even in the case of non-development, an upper-level warm anomaly associated with the weak surface low was captured by the channel 3 brightness temperature pattern. In this case,

26

however, the brightness-temperature anomaly did not intensify. From the results of his qualitative study, Velden (1992) suggested that the channel 3 MSU analyses could be used to track and monitor the upper-level thermal pattern and, hence, the evolution of baroclinic waves and cyclones, especially over conventional data-sparse regions.

Clearly, the channel 3 MSU brightness temperature anomaly signature should be highly correlated with upper-level thickness and temperature anomalies as its weighting function encompasses the mid-troposphere to lower stratosphere peaking near 300 mb. However, the hydrostatic analysis of Hirschberg and Fritsch (1991a,b; 1993a) suggests that the spatial locations and relative intensities of lower-stratospheric warm pools should also reflect the positions and relative strengths of synoptic-scale upper-level geopotential and vorticity features. Such correlations would provide important additional nowcasting and forecasting information, especially at off-synoptic times and over data-sparse regions. Specifically, the ability of the channel 3 MSU data to locate and track tropopause-level PV anomalies would be of particular value since these anomalies have been shown (Hoskins et al., 1985) to encapsulate dynamic information about the atmosphere. To address this issue, this study extends Velden's qualitative comparison by statistically correlating the channel 3 MSU brightness-temperature patterns with an expanded number of conventionally-derived fields over a six-month time period.

III. METHODOLOGY

Two methods of processing and analyzing MSU data against conventionally-derived analyses are presented in this study. The first method involves the processing and analysis of data over a six-month period to ensure that a statistically meaningful sample was analyzed. The second method involves local collection and analyses of the fields of interest in near real time. The local procedure for collection of data and its subsequent post-processing and analysis is given in Chapter V. This chapter will concentrate on the analysis procedure for the six-month dataset. However, general procedures (limb correction), which will be discussed later in this chapter, are applicable to either method.

A. DATA COLLECTION AND PRE-PROCESSING

1. Satellite Characteristics

As discussed by Rao et al. (1990), the NOAA-11 and NOAA-12 satellites are the latest in the series of polar orbiting satellites. These orbits are typically near-circular sun-synchronous with altitudes of approximately 833 km and 870 km. The orbits are staggered to minimize collection conflicts and have near orthogonal orbital planes. As a result, one satellite has a southbound equator crossing time of 0730 Local Standard Time (LST) (the "morning satellite") while the second satellite has a northbound equator crossing of 1340 LST (the "afternoon satellite"). Constant equator crossing times are ensured by placing the satellites in high inclination orbits of about 98°. This causes the individual orbits to precess eastward at the same rate (0.986° per day) that the earth moves around the sun. This precession makes for consistent scene illumination and ensures uniform observations. It also

aids in the efficient control of the satellite by ground stations. The orbital period of each satellite is about 101 minutes. A typical POES orbit is shown in Figure 9.

2. Calibration of the MSU

a. *Pre-launch and Post-launch Calibration*

MSU operations are controlled by an onboard master clock that ensures MSU scan synchronization is maintained with other onboard sensors (Rao et al., 1990). Each scan period takes 25.6 seconds and has 11 IFOVs. The antenna system of the MSU then returns to its initial starting position in readiness for the next scan line.

To provide a sound baseline for interpretation of measured radiances by the onboard radiometers both pre-launch and onboard calibration techniques are employed. Initial pre-launch calibration consists of exposure of the MSU radiometers to a known precision blackbody reference standard developed at one of the national laboratories. A relationship between the electrical output of the radiometer and the output radiance of the standard is established at this stage by varying the blackbody output in discrete steps over the dynamic range of the MSU radiometer. Even though extensive pre-launch calibration techniques are employed, radiometers can still degrade over the lifetime of the satellite. To detect and adjust for this degradation, the MSU instrument is provided with a means to calibrate itself in orbit. Onboard calibration encompasses the viewing of scenes of known radiances while in orbit. These include a brief deep space view (2.7 K) as well as a warm target view (dwell time
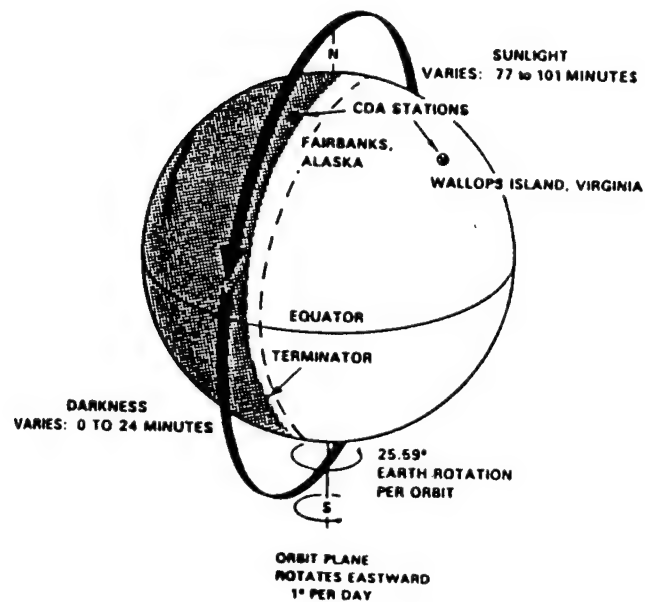
Figure 9. A typical Polar Orbiting Environmental Satellite (POES) orbit. Orbit characteristics are shown in the accompanying box. Command and Data Acquistion (CDA) are also shown. From Rao et al. (1990).

of 1.9 s) of the calibrated blackbody microwave source. The
warm target is maintained at a nominal operating temperature
of 288 K, which is the operating temperature of the MSU
radiometers (Rao et al., 1990). The warm target temperature
is controlled through use of a redundant system of platinum
resistance thermometers (Spencer et al., 1990). Onboard
calibration is performed once per scan and the calibrated
radiometer temperature outputs are then multiplexed onto the
telemetry data stream for follow-on ground-based processing.

b. *Post-captured Data Calibration Techniques*

Ground-based facilities complete the calibration of
the digitized MSU radiometer outputs and converts the measured
radiance counts to a brightness temperature. As outlined in
Spencer et al. (1990), this involves three general steps.
First, nonlinearities in instrument response to the various
instrument views (deep space, earth target, warm target) are
corrected. This is accomplished through use of the National
Environmental Satellite Data and Information Service (NESDIS)
quadratic count correction equations. These equations are
based on the pre-launch calibration measurements and have the
general form of

$$C = a_1 + C_{raw}(a_2 + a_3 C_{raw}),$$ (17)

where C is the corrected count value, C_{raw} is the raw count
value, and the a_i are coefficients that are developed in the
pre-launch calibration process and vary between satellites and
MSU channels. This correction is applied to all radiometer
counts (earth, deep space, and warm target).

The second step involves the conversion of the
measurements of the blackbody's platinum resistance network to
temperatures. This step involves conversion of the warm
target digital counts to resistances then conversion of these

32

resistances to temperatures. Since the MSU has two warm targets, one for channels 1 and 2 and one for channels 3 and 4, the average temperature of the warm targets is used. Additionally, the use of two warm targets outputs provides a measure of scan line contamination that can be based on the difference between the two outputs. Spencer et al., (1990) utilize a difference of 2° C as their basis for discarding a scan line due to possible contamination. The conversion from digital thermometer to resistance counts uses

$$R = k_0 + k_1 \left[\frac{(C_{tgt} - C_{cal_{lo}})}{(C_{cal_{hi}} - C_{cal_{lo}})} \right] , \qquad (18)$$

where R is the resistance, k_0 and k_1 are conversion coefficients and are the same for all MSUs. The parameter C_{tgt} is the radiometer digital count that has previously been corrected by equation (17). The symbols $C_{cal_{lo}}$ and $C_{cal_{hi}}$ represent the precision resistance counts of the onboard warm target circuitry, respectively. Conversion from resistance to target temperatures is accomplished through use of equation (18) with instrument-specific data provided by the Jet Propulsion Laboratory (JPL) and through use of another set of equations developed by NESDIS. The general form of these equations is

$$T_{tgt} = e_0 + R(e_1 + e_2 R) , \qquad (19)$$

where T_{tgt} is the temperature of the "target", the e_i's are resistance to temperature coefficients that are both satellite and instrument specific, and R is resistance measurement from equation (18).

Lastly, brightness temperatures are calculated by interpolation of the converted temperatures between the

33

corrected counts of deep space and the various targets via the following equation,

$$T_b = \frac{(T_{tgt} - 2.7K) \, x \, (C_{earth} - C_{space})}{(C_{target} - C_{space})} + 2.7 \, . \tag{20}$$

The ground-based processing provides four independently calibrated brightness temperature measurements corresponding to the four MSU channels. Grody (1983) states that the calibration of the instrument provides an almost linear relationship between the radiometer response to the measured "warm" target temperature and cold space. Brightness-temperature fluctuations (noise) in the MSU instrument is reduced to 0.3 K through the calibration procedure (0.1 s integration time) (Grody, 1983). Due to insufficient dwell time between the space view and the warm-target view small scan- to- scan biases can develop that lower the accuracy of the brightness-temperature retrievals (Spencer et al., 1994). The elimination of these biases can be accomplished by averaging the calibration data over 3 scan lines according to Spencer et al. (1994). The data used in the climatology portion of this study utilized the 3-scan averaging procedure developed by Spencer et al. (1994) as mentioned above. However, the local collection of MSU data (described in the Appendix) utilizes a scan- to- scan calibration technique and, thus, would be expected to include some scan- to- scan bias.

3. MSU Limb Correction Techniques

As the MSU scans from nadir to the edges of its swath limit, there is an apparent increase in the height (decrease in pressure) at which the weighting functions for all MSU channels peak (Fig. 7). This phenomena equates to a decrease in the sensed radiance of a target which, in turn, produces a

correspondingly lower than actual brightness temperature. The "limb darkening" effect results from the combined effect of the longer path length that the microwave energy must travel from the target to the sensor (Grody, 1983), as well as from sidelobe effects at the extreme scan angles (Koehler, 1989). The sidelobe effects are a result of the diffraction pattern created by the MSU antennas. These patterns can allow cold space energy to be sensed at the MSU radiometers via the sidelobes. At the extreme edges of the swath it produces a 30% decrease in the pressure at which the weighting functions peak (Grody, 1983). Two general methods have been developed for handling this problem. The first is a limb-correction procedure where correction coefficients are applied to correct the slant path radiance to a nadir reference, and then a nadir form of the radiative transfer equation (RTE) is solved (Le Marshall and Schreiner, 1985). It should also be mentioned here that correction to footprints other than nadir is possible. This will be discussed below. The second technique is physically based. In this case, the solution to the RTE has the physical effects of slant path built into the equation.

The statistically-based limb correction technique is in common use today. Limb correction coefficients are developed by NESDIS utilizing synthetic radiances computed from a global set of atmospheric temperature and moisture profiles. This procedure is outlined by Werbowetzski (1981). These coefficients are periodically distributed to users in Tiros-N Operational Vertical Sounder (TOVS) export packages along with upgrades in processing software.

The limb-correction coefficients account for off-nadir scan angles and the surface emissivity differences between land and water that are evident at microwave frequencies. Thus, the first step in the limb-correction process is a check of the geographic location of the satellite footprints. Then

the proper set of limb-correction coefficients for each channel are extracted based on either an over land or over water footprint. These are applied to the MSU observations to develop corrections that are then added to the original observations (Koehler, 1989).

Physically-based limb correction involves incorporation of an angle-dependant transmittance term in the radiative transfer equation (RTE) that has modelled limb effects built into it. This term describes the increased opacity of the atmosphere between the target and the MSU due to the longer path lengths. Le Marshall and Schreiner (1985) conducted a study that compared a statistically-based limb-correction scheme (similar to the currently operational scheme) against a physically-based scheme. They found little difference between the two schemes over the near-nadir footprints. However, the differences became more pronounced at the edges of the swath. Differences were also more pronounced in the low- to- mid troposphere where temperature gradients associated with frontal features are more intense. By 250 mb, the difference between the two schemes was not as evident. On the basis of this study, Le Marshall and Schreiner (1985) concluded that the physically-based retrieval scheme was better at maintaining coherency of strong temperature gradients at large angles.

Ideally, it is desirable to have a full physically-based solution of the RTE that precludes the use of limb-correction coefficients. Unfortunately, such a solution was not available for either the climatological MSU data set that is the focus of this study, nor the locally-collected data. A disadvantage of determining the full RTE solution is that it is costly in computer time especially when compared to the use of the statistical correction technique. Since the purpose of this study is more concerned with the correlation of the MSU channel 3 brightness temperature with various conventionally-

derived fields within the mid- to- upper-troposphere and lower-stratosphere, a statistical limb correction was assumed sufficient.

When using the statistically-based technique, correction to intermediate footprints vice nadir can ameliorate the magnitude of the error inherent in the limb-correction scheme (Le Marshall and Schreiner, 1985). This comes about because a smaller limb correction is needed at the intermediate footprints. The six months of MSU data utilized in this study were corrected to intermediate angles of 33° vice nadir in a technique developed by Spencer et al. (1994). The angle corresponds to scan positions 3 and 9 (Fig. 8). Sets of limb-correction coefficients were developed by Spencer et al. (1994) by multiple linear regression of brightness temperatures based on latitude, month and satellite. These were utilized to correct the brightness temperature to the 33° incidence angle by regressing the average of the 3rd and 9th footprint against the other footprint's average brightness temperature values via the following equation

$$T_b{}^* = a_0 + a_2 T_{b2} + a_3 T_{b3} + a_4 T_{b4}, \tag{21}$$

where $T_b{}^*$ is the channel 3 MSU brightness temperature corrected for the view angle, the a_i's are the regression coefficients developed for each MSU channel and the T_{bi}'s are the measured MSU channel brightness temperatures. The authors use the three upper-MSU channels to provide the scan angle correction necessary to adjust for the effects of non-nadir scan positions.

B.   FOLLOW-ON DATA PROCESSING: THE SIX MONTH DATASET

NOAA-11 and NOAA-12 global MSU brightness-temperature data for the period between 1 October 1993 and 31 March 1994

37

were obtained from the Marshall Space Flight Center. The statistical analysis began with the daily extraction of those satellite passes that fell between 25° N and 65°N and within a 1.5 hour window on either side of 0000 UTC and 1200 UTC during this six-month period. A consistent approximately 2K bias between NOAA-11 and NOAA-12 (NOAA-12 warmer than NOAA-11) was corrected by applying latitudinally-smoothed offsets to the NOAA-12 channel 3 MSU brightness temperatures. These offsets were calculated by first averaging each satellite's (NOAA-11, NOAA-12) channel 3 MSU brightness temperatures over 10° wide global-latitude bands for each month (October 1993 - March 1994). Erroneous and missing values were excluded from the average. Then, the latitudinally averaged NOAA-11 brightness temperatures were subtracted from the NOAA-12 monthly-averaged brightness temperatures creating offsets. Finally, the offsets were applied to each of the NOAA-12 channel 3 MSU brightness temperatures at each time. A multiquadric interpolation scheme (Nuss and Titley, 1994) was then used to objectively analyze the extracted channel 3 MSU data on a regular 2.5° latitude by 2.5° longitude (145 x 17) grid centered at 45° N, 180° W for each 0000 UTC and 1200 UTC map time. The multiquadric scheme was initially developed by Hardy (1971) primarily for mapping and geodesy purposes. It uses radial hyperboloid functions to fit scattered data to the regular grid and has been found by Nuss and Titley (1994) to be more accurate than either the Cressman or the Barnes objective analysis schemes in tests of analytic functions.

Corresponding 12-h conventional analyses of the fields listed in Table 2 were obtained from the National Meteorological Center's Global Data Assimilation System (GDAS) on the same grid at mandatory levels. Derived fields of vorticity, potential vorticity, dynamic tropopause (see Chapter II) and thickness were calculated with these conventional analyses. These fields were chosen for several

1.	Sea-level Pressure (mb)
2.	1000 - 500 mb Thickness (mb)
3.	400 - 100 mb Thickness (mb)
4.	250-mb Temperature (°C)
5.	200-mb Temperature (°C)
6.	500-mb Height (Dm)
7.	400-mb Height (Dm)
8.	100-mb Height (Dm)
9.	50-mb Height (Dm)
10.	500-mb Vorticity (10^{-5} s^{-1})
11.	100-mb Vorticity (10^{-5} s^{-1})
12.	300-mb Isentropic Pot. Vorticity (10^{-6} m^2 s^{-1} K kg^{-1})
13.	Dynamic Tropopause (1.5×10^{-6} m^2 s^{-1} K kg^{-1})

Table 2. Conventional fields obtained from the National Meteorological Center's GDAS.

reasons. First, they represent important quantities associated with cyclogenesis. In particular, the fields of 300-mb potential vorticity and the dynamic tropopause are useful in the application of PV thinking to cyclogenesis. The height fields and vorticity were chosen because they represent traditional fields of interest. In addition, correlation of height anomalies with MSU anomalies allows the investigation of the validity of the LID assumption (Hirschberg and Fritsch, 1991a). The 400 - 100 mb thickness relates to the layer-mean

temperature that the MSU channel 3 brightness temperature should equate to, and, therefore, be highly correlated with.

1. Statistical Correlations

Two sets of six-month correlations were compiled. The first were spatial correlations between the channel 3 MSU brightness temperature and the conventional (Table 2) analyses for each 12-h map time. The second involved calculating temporal correlations between the 12-hourly channel 3 MSU brightness temperatures and the conventional data at individual grid point locations. Since the procedure for deducing the spatial and temporal correlations were different, they will be discussed separately.

a. *Spatial Correlations*

Spatial correlation coefficients between the channel 3 MSU brightness temperature and the conventional analyses were calculated for every available 12-h map time over the six-month period. Specifically, the correlations were calculated for eight 30° x 30°(13 x 13 grid points) sub-domains or areas (Fig. 10). The domains were chosen to compare data-sparse regions with data-rich regions (Fig. 10). This subdivision also allowed for a gross evaluation of the effects of surface type (land versus water) as well as terrain effects on the correlations.

There were a possible 364 (0000 UTC and 1200 UTC) map times during the six months. However, not all of these times (depending on area) were available for processing owing to the criterion that the NOAA 11 or NOAA 12 satellite pass time over an area had to be within a ± 1.5-h window around 0000 UTC or 1200 UTC. In addition, a criterion that at least 75% of the area of interest had to be covered by satellite

40
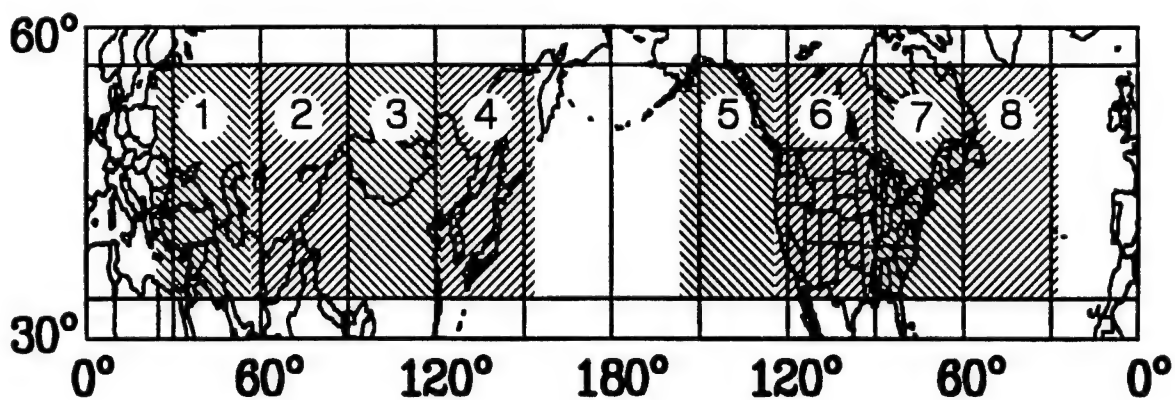
Figure 10. Map of the climatology domain used in the calculation of spatial correlations for each map time between the channel 3 MSU brightness temperature and various conventionally-derived fields. Stippled regions with numbers indicate the 8 areas over which spatial correlations were calculated.

41

observations at each valid time was applied. This requirement further reduced the number of available map times. Accordingly, a total of between 199 and 354 out of the possible 364 map times were analyzed over the six-month period depending on the area (Table 3). In particular, over 50% of

AREA	TOTAL AVAILABLE MAPS
1	211
2	352
3	343
4	199
5	211
6	354
7	342
8	206

Table 3. Total map times available for calculation of spatial correlation coefficients between the channel 3 MSU and selected conventional fields.

the available map times were used in the calculation of the spatial correlation coefficients for areas over western Asia and the Pacific and North Atlantic oceans. Better than 90% coverage was obtained over Central Asia and North America. Additionally, owing to the specific orbital paths, most of the channel 3 MSU data were obtained for the 12 UTC map time "window" for sub-domains 1 and 8. Conversely, the Pacific region (areas 4 and 5) primarily used MSU data within the 0000 UTC "window". Other areas (Central Asia, North America) had an even mix of both 0000 UTC and 1200 UTC MSU channel 3 data over the six months. Fortunately, as will be shown in Chapter 4, the map time distribution appears not to

have had an effect on the average spatial correlation coefficients that were calculated. It was also of interest to investigate scale dependencies present in the data. The size (2400 km x 3300 km) of the eight sub-domains provided a "natural" filter for synoptic-scale features upon removal of latitudinal and longitudinal trends in the data. In particular, each area analysis was decomposed into two portions, a large scale or trend portion and a small scale or detrended potion. The detrended portion was formed following the method of Errico (1985). This procedure removes the effect of the larger-than-synoptic-scale waves. First, for each j, the slope of the surface was computed by

$$s_j = \frac{a_{N_I,j} - a_{1,j}}{N_I - 1} .$$ (22)

where s_j is the slope of the jth longitude and N_I is the maximum width of the sub-domain. In the present case $N_I = 13$. Next, the trend in the i direction was removed for each i,j through

$$a'_{i,j} = a_{i,j} - \frac{1}{2} (2i - N_I + 1) s_j,$$ (23)

where $a'_{i,j}$ is the grid point detrended in the longitudinal direction and the other variables are as before. Finally, the roles of i and j are reversed to detrend the data in the latitudinal direction with the $a'_{i,j}$ from equation (23) replacing the $a_{i,j}$ in equation (22) to obtain a new field detrended in both latitude and longitude. The result is

43

periodic with wavelengths less than or equal to the domain size. That is

$$a^N_{i,1} = a^N_{i,N_j},\qquad (24)$$

for all i, with $N_j = 13$, and

$$a^N_{1,j} = a^N_{N_1,j},\qquad (25)$$

for all j. The trended or large-scale portion of the analysis was recovered by subtracting the detrended analysis from the full analysis. An example from Errico (1985) of full, trend and detrend analyses is shown in Figure 11.

Correlations were compiled for the full, trended and detrended analyses for each available map time and each area. The correlation coefficients for a particular map time were calculated with

$$\rho_a = \rho(m,c) = \frac{Cov(m,c)}{\sqrt{V(m)\,V(c)}},\qquad (26)$$

where ρ_a is the area correlation coefficient, $Cov(m,c)$ is the covariance of the MSU data and conventionally derived data at each grid point i,j for each map time, and $V(m)$, $V(c)$ are the variances of the MSU data and conventional data over the subdomain. Prior to calculation of the correlation coefficient with equation (26) the data was de-meaned by removal of the subdomain mean from the fields. A correlation criteria of ≥ 0.80 between the 400-100 mb thickness and the MSU was also utilized to segregate the correlation results into potentially "good" and "bad" candidate analysis categorizations. Finally, six-month-average correlation coefficients were determined for each area by summing the available 12-h coefficients over the six months and dividing by the number of analysis times.

44
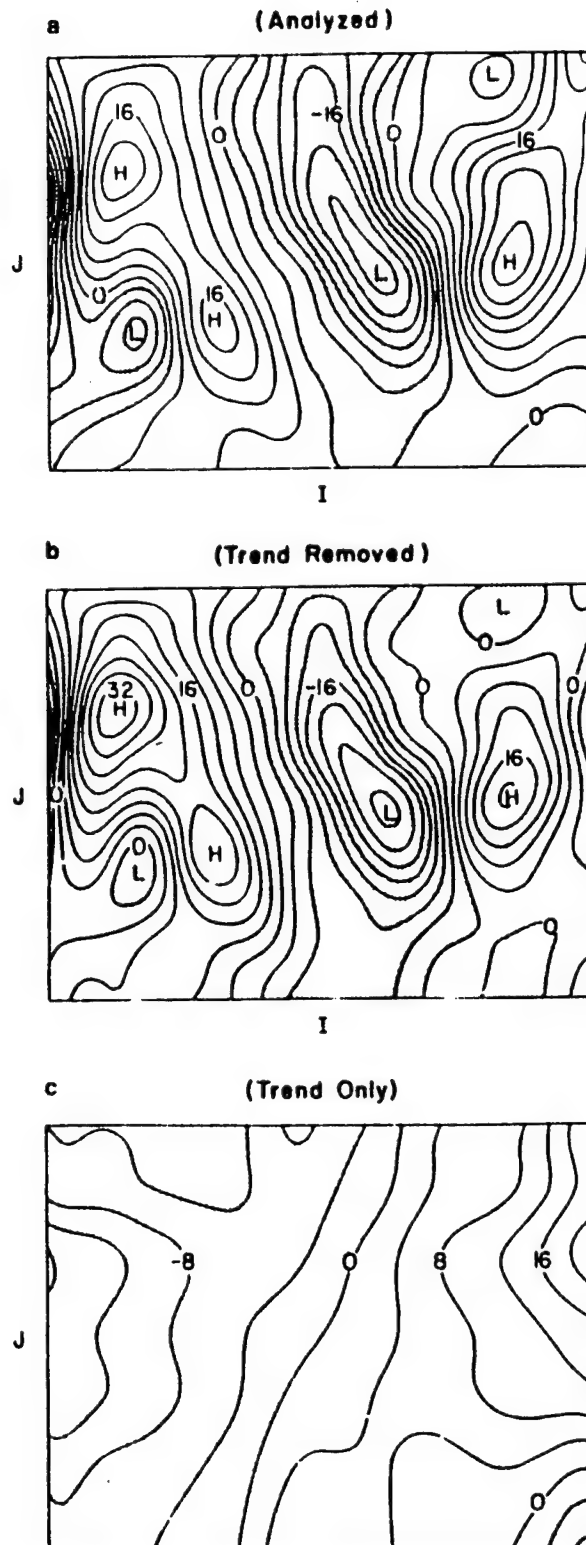
Figure 11. Examples of velocity field that (a) contains the total field (trend), (b) the velocity field with the trend removed, and (c) the velocity field with only the trend remaining. From Errico (1985).

45

b. Temporal Correlations

The temporal correlation coefficients were calculated only at the grid point locations containing at least 115 days (330 12-h values) of satellite data (Fig. 12). To determine the temporal correlations at the grid point locations, the channel 3 MSU brightness temperatures and conventional data were first normalized by applying the following function,

$$f_{i,j,t} = \frac{f'_{i,j,t} - \overline{f'}}{\overline{f'}} \qquad (27)$$

to the temporal series at each grid point i,j. In (27), $f'_{i,j,t}$ is the normalized value of the variable $f_{i,j,t}$ over all times (nt).

The correlation coefficients were then calculated with

$$\rho_{i,j} = \rho\,(m,c)_{i,j} = \frac{Cov(m,c)}{\sqrt{V(m)\,V(c)}}, \qquad (28)$$

where $\rho_{i,j}$ is the temporal correlation coefficient between the channel 3 MSU brightness temperature (m) and the conventional data (c) series of interest at grid point i,j. In (28) Cov is the covariance and V is the variance.

To investigate scale dependencies in the data, high- and low-pass elliptical filters were applied to the time series at each grid point. Wave periods were selected that produced synoptic-scale filtered series and longer than synoptic-scale filtered series. The time scales used to distinguish these periods agree with the classification schemes developed by Orlanski (1975) and Fujita (1986). The low-pass filter was designed to pass waves with periods longer than 14 days (longer than synoptic-scale) while a separate

46
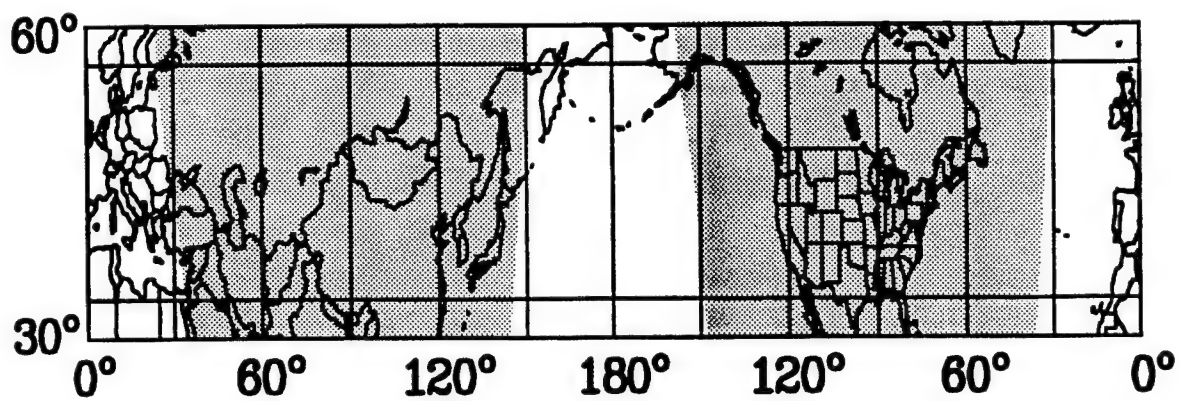
Figure 12. Climatological domain (stippled) used in the calculation of correlations between channel 3 MSU and various conventional-derived fields.

high-pass filter was designed to pass waves with periods shorter than 5 days (synoptic-scale).

According to Yates and Bateman (1989), the elliptic filter provides excellent attenuation compared to other filters (e.g. Butterworth, Chebyshev) for a given filter order. A lower filter order allows for the filtering of time domain signals in less computer time as the rate of convergence for the function increases (Murakami, 1979). However, a drawback of the elliptic filter is the poor phase response (Yates et al., 1989). Obviously, phase errors introduced by the filtering process would add to the other errors in the processing and would contaminate the correlations. Fortunately, there are techniques that can be applied to the filtering process that reduce the phase errors induced by the use of finite time series with a finite transit start up time. This problem was alleviated in the six-month data set by first padding the start and end times of the series with zeros for averaging purposes. Then, the series was "normally" filtered (i.e. forward in time), followed by a second pass where the output of the forward filtering step was reversed in time and again passed through the filter. The above steps produced a filtered series where all frequencies had zero phase shifts. An example of unfiltered, low-pass, and high-pass filtered MSU time series is presented in Figure 13.

Correlation coefficients at each grid point were then calculated over the series duration with equation (27). The correlations for the unfiltered and low and high-pass filtered series were then mapped to the same 2.5^0 by 2.5^0 regular grid to produce analyses of "time correlations". In both the spatial and temporal calculations, a student's T-test was used to verify that the correlations were statistically significant.
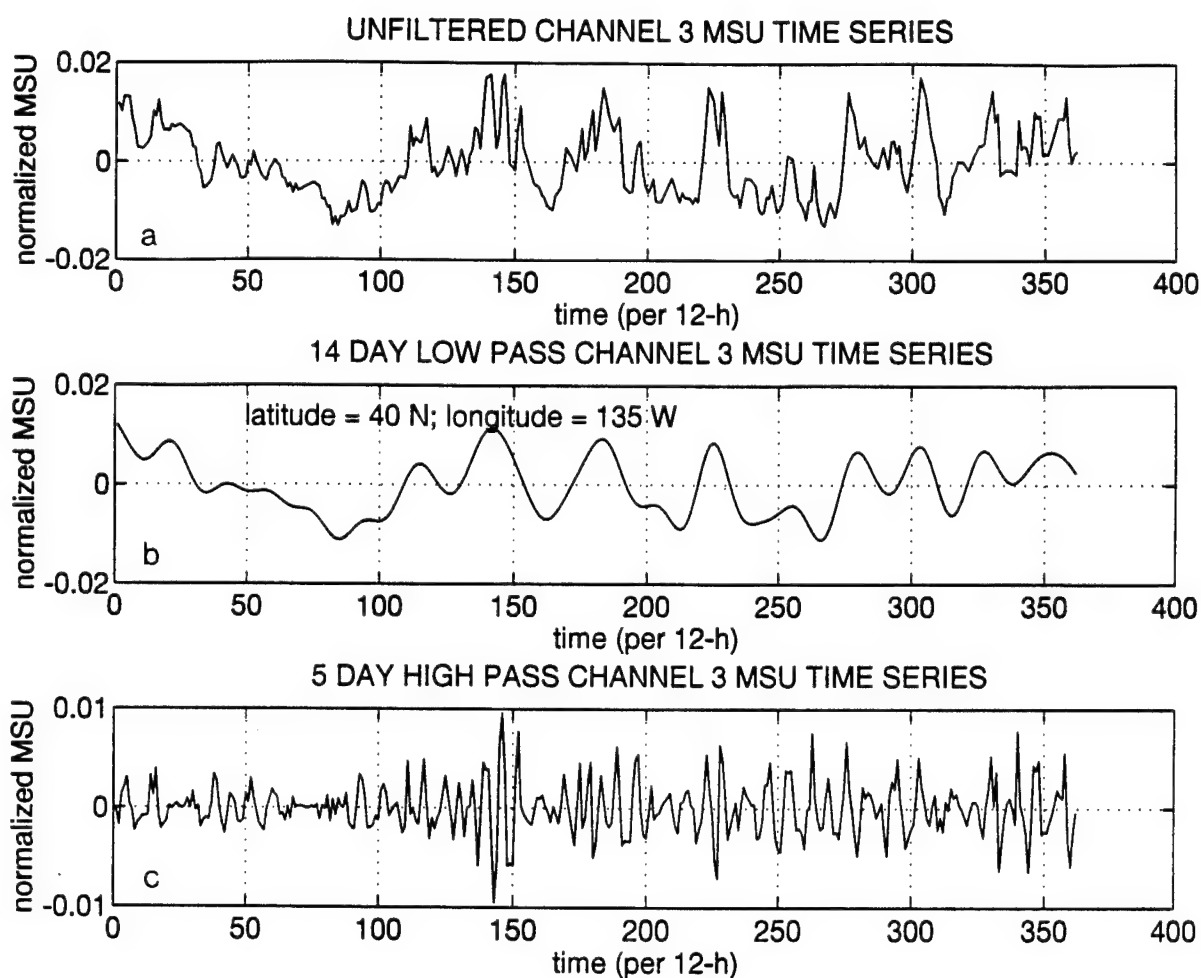
Figure 13. An example of the time filtering of the channel 3 MSU at an individual grid point. (a) unfiltered series, (b) 14 day low-pass filtered (> synoptic scale) series, and (c) 5 day high-pass (≤ synoptic scale) series.

49

IV. RESULTS

In this chapter, the six-month spatial and temporal correlation coefficients between the channel 3 MSU and the conventional analyses (see Table 2) are presented. Since there were redundancies in the MSU-conventional correlations when comparing similar conventional fields (e.g., the MSU 500-mb height and MSU 400-mb height correlations) we limit the presentation and discussion of the results to only those MSU-conventional analysis comparisons found to be most significant.

A. SPATIAL CORRELATIONS

The six-month average spatial correlation coefficients between the channel 3 MSU and the 400 - 100 mb thickness, 500-mb height, 50-mb height, 500-mb vorticity, 200-mb temperature, dynamic tropopause, and sea-level pressure for each of the eight areas (Fig. 10) are presented in Tables 4 through 10, respectively. In these tables, the coefficients are broken down into various categories. These categories are correlations determined with the TOTAL, DETREND, and TREND analyses. In addition, the correlations are grouped according to those map times when the total MSU 400-100-mb thickness correlation was $\geq$ 0.80, and < 0.80, as well as for all available times. The motivation for this subdivision will be discussed below.

1. MSU and 400 - 100 mb Thickness

Since the MSU channel 3 represents a layer-averaged brightness temperature between 400 - 100 mb, it is not surprising to find generally high positive average

51

correlations between the MSU channel 3 and 400-100-mb thickness analyses for all domains and horizontal scales (Table 4). In particular, the complete (TOTAL) analysis correlations with all times (AT) considered range between 0.84 (Area 8-northwestern Atlantic) and 0.92 (Area 4-east Asia and adjacent waters). For the "large scale" TREND analyses, the correlations range between 0.83 (Area 8-northwestern Atlantic) and 0.95 (Area 3-central Asia). Less positive correlation coefficients are found, particularly over the Eastern Hemisphere (EH), in the "small scale" DETREND analyses 0.69 in Area 3 with the highest correlations found over areas 7 and 8 (corresponding to eastern North America and the northwestern Atlantic).

When 12-h map times are partitioned according to whether the total MSU 400-100-mb thickness correlation coefficient is ≥ 0.80, there is an increase in the average correlation coefficients across all horizontal scales and sub-domains. This segregation of map times was done in an attempt to identify potentially "good" and "bad" analysis times. The supposition was made that correlations between the MSU and the other conventional fields (e.g., 500-mb height) would suffer and be suspect if the MSU 400-100-mb thickness correlation was poor (<0.80). Fortunately, the application of this "thickness correlation criteria" (TCC) to the TOTAL and TREND fields resulted in an average of about 83 % of the map times showing relatively high (≥ 0.80) MSU 400-100-mb thickness correlation. This result indicates that the MSU channel 3 exhibits a high degree of spatial correlation compared with the conventionally-derived thickness field when considering all wavelengths within a sub-domain (TOTAL field) or when compared only against wavelengths that are longer than the sub-domain size (TREND field). In the case of the DETREND analyses, the subjection of the TCC ≥ 0.80 criteria also increases the magnitude of the average correlation value in

52

AREAS	TOTAL	DETREND	TREND
1. AT CRITERIA	0.86	0.78	0.87
TCC ≥0.80	0.91 (78%)	0.89 (60%)	0.94 (81%)
TCC ⟨0.80	0.68 (22%)	0.61 (40%)	0.55 (19%)
2. AT CRITERIA	0.89	0.73	0.92
TCC ≥0.80	0.92 (80%)	0.88 (50%)	0.96 (91%)
TCC ⟨0.80	0.60 (20%)	0.58 (50%)	0.58 (09%)
3. AT CRITERIA	0.90	0.69	0.95
TCC ≥0.80	0.93 (88%)	0.87 (35%)	0.96 (97%)
TCC ⟨0.80	0.68 (12%)	0.60 (65%)	0.69 (03%)
4. AT CRITERIA	0.92	0.82	0.93
TCC ≥0.80	0.94 (92%)	0.90 (69%)	0.95 (92%)
TCC ⟨0.80	0.69 (08%)	0.64 (31%)	0.70 (08%)
5. AT CRITERIA	0.88	0.85	0.87
TCC ≥0.80	0.91 (85%)	0.90 (80%)	0.92 (82%)
TCC ⟨0.80	0.67 (15%)	0.65 (20%)	0.62 (18%)
6. AT CRITERIA	0.88	0.88	0.86
TCC ≥0.80	0.92 (83%)	0.91 (88%)	0.93 (79%)
TCC ⟨0.80	0.68 (17%)	0.62 (12%)	0.59 (21%)
7. AT CRITERIA	0.86	0.88	0.83
TCC ≥0.80	0.93 (80%)	0.93 (84%)	0.94 (76%)
TCC ⟨0.80	0.57 (20%)	0.65 (16%)	0.49 (24%)
8. AT CRITERIA	0.84	0.83	0.83
TCC ≥0.80	0.92 (78%)	0.91 (74%)	0.93 (73%)
TCC ⟨0.80	0.57 (22%)	0.62 (26%)	0.56 (27%)

Table 4. Six-month-average spatial correlation coefficients between the channel 3 MSU brightness temperature and 400-100-mb thickness analyses for the eight areas. The coefficients are categorized according to whether corresponding TOTAL, DETREND, or TREND MSU-thickness analyses were utilized in the correlation calculation. The coefficients are also categorized for those times when the total MSU-400-100-mb thickness correlation TCC was ≥ 0.80, < 0.80, and for all available times (AT). The percentage of available map times used in the calculation of the correlation coefficients for the ≥ 0.80 and < 0.80 groups is provided in parenthesis.

53

each sub-domain. However, the percentage of map times meeting the above criteria significantly decreases over the Eurasian and Asian continents. For instance in Area 1, the percentage of good (TCC $\geq$ 0.80 criteria) map times decreases to 60%. This decrease is also found in Area 3 where only 35% of the map times meet the criteria. Thus, since the DETREND field consists of those synoptic-scale and shorter wavelengths that are resolvable within the sub-domain area, it appears that these wavelengths were not well described for much of the time by the MSU channel 3 in these areas. Significantly, the percentage of "good" map times for the DETREND field increases from the relatively low percentages found across the first four sub-domains to 80% in the Eastern Pacific. Across the North American continent the percentages continue to increase to 88% for Area 6 and 84% for Area 7 and, then decrease to 74% across Area 8 (northwest Atlantic). There is also a significant increase in the correlation coefficient average to slightly above 0.90 in the DETREND fields across the Western Hemisphere (WH) for the good cases. Thus, in a spatial sense, the MSU channel 3 brightness temperature patterns were highly correlated with the 400-100-mb thickness patterns at the majority of the map times from the Eastern Pacific to the Northwestern Atlantic.

When evaluating only those map times when the total MSU 400-100-mb thickness correlation was < 0.80 (the bad candidates), both the percentage of map times and the average correlations generally decreased in all fields across all sub-domains. The DETREND field for Areas 2 and 3 has a relatively high percentage of bad map times (< 0.80 criteria) of 50% and 65%, respectively. This result is not entirely clear although some hypotheses will be presented later that concern the apparent discrepancies in the correlation results over the eastern European and Asian continents.

54

2. MSU and 200 mb Temperature

The relatively high correlations between the MSU and 400-100-mb thickness analyses suggest that the MSU should also be highly correlated with isobaric temperature patterns within the layer. Hirschberg and Fritsch (1991a,b) find the strongest temperature anomalies associated with tropopause undulations to be near 200 mb. The six-month results (Table 5) do suggest that the MSU is positively correlated with the 200-mb temperature pattern but not as well as with the layer-average temperature reflected by the 400-100-mb thickness. Specifically, the strongest correlations (average = 0.77) occur in the DETREND fields with the TCC $\geq$ 0.80 applied.

This result is in agreement with the findings of Velden (1992) who qualitatively demonstrated the correlation between warm anomalies in the MSU channel 3 brightness temperature and upper-level temperature analyses during selected cyclone cases. Unlike Velden's findings, however, the six-month results suggest that the strongest positive correlations between the MSU and a single isobaric temperature analysis lie at 200 mb rather than at 250 mb (not shown). The overall geographic distribution of correlations is similar to Table 4 with highest correlations in the North American area land lowest in Area 3, central Asia. Significantly, the high positive correlations found here in the six-month data set suggest that the MSU channel 3 brightness temperature analyses can be utilized to track synoptic-scale tropopause-level thermal anomalies with a high degree of confidence.

3. MSU and 500 mb and 50 mb Height

The potential utility of the MSU in enhancing the dynamical understanding and forecasting of baroclinic systems is perhaps better illuminated by examining the correspondence

55

AREA	TOTAL	DETREND	TREND
1. AT	0.55	0.59	0.55
TCC ≥ 0.80	0.62	0.76	0.66
TCC < 0.80	0.28	0.34	0.06
2. AT	0.62	0.57	0.70
TCC ≥ 0.80	0.69	0.76	0.77
TCC < 0.80	0.16	0.39	0.01
3. AT	0.61	0.50	0.74
TCC ≥ 0.80	0.67	0.75	0.76
TCC < 0.80	0.18	0.38	0.37
4. AT	0.73	0.65	0.75
TCC ≥ 0.80	0.78	0.76	0.80
TCC < 0.80	0.23	0.41	0.23
5. AT	0.78	0.76	0.76
TCC ≥ 0.80	0.82	0.82	0.81
TCC < 0.80	0.55	0.55	0.52
6. AT	0.69	0.74	0.63
TCC ≥ 0.80	0.75	0.79	0.73
TCC < 0.80	0.41	0.35	0.26
7. AT	0.57	0.68	0.52
TCC ≥ 0.80	0.70	0.76	0.67
TCC < 0.80	0.07	0.27	0.06
8. AT	0.61	0.62	0.57
TCC ≥ 0.80	0.72	0.72	0.72
TCC < 0.80	0.22	0.35	0.15

Table 5. As in Table 4, except for MSU and 200-mb temperature correlations.

between the MSU brightness temperature and geopotential height patterns at individual isobaric levels. The relationship between isobaric-layer temperature anomalies and geopotential height anomalies that bracket the layer depends on how the associated temperature (thickness) anomaly is spread hydrostatically in the vertical. For instance, a warm anomaly between 400 mb and 100 mb would result in a positive geopotential height anomaly at 100 mb (higher heights) if the 400-mb geopotential field was relatively uniform (no anomalies). Conversely, such a warm anomaly would result in a negative geopotential height anomaly at 400 mb (lower heights) if the 100-mb geopotential field was relatively uniform.

Hirschberg and Fritsch (1993b) suggest that the direction and degree of influence of these anomalies (thickness spreading) is scale dependent. In particular, they demonstrate with an analytic model that the spreading occurs downward for flows with synoptic-scale wavelengths less than approximately 5000 km and increasingly upwards for larger scale flows. They use this scale dependence argument to hypothesize the existence of a stratospheric level of insignificant dynamics (LID) where the geopotential height tendencies at synoptic space and time scales are insignificant (Hirschberg and Fritsch, 1991a,b; Hirschberg and Fritsch 1993a,b; Hirschberg and Fritsch 1994). Given the existence of a LID, they explain how upper-level temperature anomalies associated with synoptic-scale undulations in the tropopause can hydrostatically induce height and height tendency anomalies below them.

Based this scale-dependency argument, we should expect to find that the DETREND (smaller-scale) MSU patterns are more highly negatively correlated with mid-level geopotential height patterns and the TREND (larger-scale) MSU patterns are more highly positively correlated with upper-level

57

geopotential height patterns. To investigate these relationships, we next examine the average spatial correlations between the MSU channel 3 brightness temperatures and the conventionally-derived 500-mb and 50-mb height analyses that are presented Tables 6 and 7.

AREA	TOTAL	DETREND	TREND
1. AT	0.49	−0.58	0.72
TCC ≥0.80	0.49	−0.75	0.77
TCC ⟨0.80	0.46	−0.34	0.49
2. AT	0.63	−0.56	0.80
TCC ≥0.80	0.62	−0.72	0.81
TCC ⟨0.80	0.64	−0.40	0.73
3. AT	0.65	−0.52	0.75
TCC ≥0.80	0.64	−0.70	0.75
TCC ⟨0.80	0.68	−0.42	0.67
4. AT	0.23	−0.79	0.50
TCC ≥0.80	0.22	−0.84	0.49
TCC ⟨0.80	0.30	−0.69	0.56
5. AT	−0.75	−0.84	−0.64
TCC ≥0.80	−0.77	−0.88	−0.64
TCC ⟨0.80	−0.61	−0.69	−0.55
6. AT	−0.36	−0.78	0.27
TCC ≥0.80	−0.41	−0.83	−0.32
TCC ⟨0.80	−0.17	−0.43	−0.07
7. AT	−0.14	−0.70	0.03
TCC ≥0.80	−0.28	−0.78	−0.07
TCC ⟨0.80	0.40	−0.31	0.35
8. AT	−0.20	−0.63	−0.01
TCC ≥0.80	−0.31	−0.73	−0.11
TCC ⟨0.80	0.17	−0.34	0.26

Table 6. As in Table 4, except for MSU and 500-mb height.

59

AREA	TOTAL	DETREND	TREND
1. AT	0.79	0.28	0.87
TCC ≥0.80	0.82	0.19	0.92
TCC <0.80	0.70	0.40	0.65
2. AT	0.83	0.23	0.91
TCC ≥0.80	0.84	0.11	0.92
TCC <0.80	0.76	0.35	0.81
3. AT	0.86	0.29	0.90
TCC ≥0.80	0.86	0.29	0.91
TCC <0.80	0.82	0.29	0.77
4. AT	0.67	0.33	0.78
TCC ≥0.80	0.68	0.35	0.78
TCC <0.80	0.52	0.27	0.73
5. AT	-0.02	-0.07	0.01
TCC ≥0.80	0.00	-0.05	0.07
TCC <0.80	-0.16	-0.12	-0.24
6. AT	0.08	0.07	0.08
TCC ≥0.80	0.04	0.05	0.04
TCC <0.80	0.28	0.28	0.25
7. AT	0.20	0.31	0.24
TCC ≥0.80	0.09	0.30	0.15
TCC <0.80	0.60	0.36	0.49
8. AT	0.13	0.23	0.22
TCC ≥0.80	0.04	0.22	0.13
TCC <0.80	0.44	0.24	0.45

Table 7. As in Table 3, except for MSU and 50-mb height.

60

The correlation coefficients pertaining to the TOTAL analyses at 500 mb exhibit mixed results (Table 6). This is to be expected since the TOTAL fields at this mid level probably reflect a full spectrum of wavelengths. In particular, over both the EH and WH there is generally poor correlation between the TOTAL channel 3 MSU and the 500-mb geopotential height analyses. The average TOTAL correlation over the EH and WH with all times considered (AT) is 0.50 and -0.36, respectively. The TREND (large-scale) correlations show relatively high positive coefficients between the channel 3 MSU and the 500-mb geopotential heights over the EH (average = 0.69). This result is difficult to interpret based on the scale-dependence hypothesis although it might be linked to thermal anomalies in lower layers of the atmosphere. Conversely, in the WH, the TREND results seem to agree with the scale-dependence argument. Specifically, the TREND 500-mb geopotential height analyses are not correlated with the channel 3 MSU (average = -0.09). Application of the TCC results in somewhat of a chaotic pattern of coefficients across the eight areas.

The DETREND (small-scale) MSU and 500-mb height analyses show consistent negative correlations across all sub-domains. In the EH with all times considered, the average correlation is -0.61 while in the WH the average increases to -0.74. Significantly the application of the TCC, that is, when the data is partitioned according to those map times that are potentially "good" (total MSU versus 400-100 mb thickness correlation ≥ 0.80) and those map times that are potentially "bad" (total MSU versus 400-100 mb thickness correlation < 0.80), illuminates even higher negative correlations between the DETREND MSU and 500-mb heights. Specifically, the correlations increase to -0.75 over the EH and -0.81 over the WH when the map times are good. The EH result is tempered somewhat by the percentage of map times available for

61

processing (see Table 4). At best, only 69% of the total available map times in the sub-domains were in the TCC ≥ 0.80 category. Percentages for the EH range from 35% to 69%. Conversely, the WH percentages were significantly higher, ranging from 74% over the Northwest Atlantic to 88% over the western United States.

Again, given the scale-dependency argument, we should expect to find that the TREND (larger-scale) MSU patterns to be more highly correlated in a positive sense with upper-level geopotential height patterns than the DETREND (smaller-scale) patterns. Since the TOTAL height field at 50-mb should reflect the large-scale wave signal, particularly in comparison to the 500-mb level, we should also see relatively high correlations between the TOTAL MSU and 50-mb height analyses as well.

In support of this, the results for the EH and WH (Table 7) are generally consistent and indicate small correlation between the DETREND MSU and 50-mb height fields. The average coefficient for the AT DETREND is 0.21. As with the analogous 500-mb trend results, application of the TCC to the DETREND 50-mb data results in an unstructured pattern of correlation responses across the sub-domains.

The TOTAL and TREND correlation results are less clear with respect to scale dependence argument. As expected, both the TOTAL and TREND AT analyses exhibit high positive correlations over the EH, with averages of 0.79 and 0.87, respectively. However, both the TOTAL (average = 0.10) and TREND (average = 0.14) AT analyses fields indicate no correlation over the WH. The discrepancy between the EH and WH results is curious and merits further consideration. When the TCC ≥ 0.80 criteria is applied for sub-domains in the EH, the correlations tend to increase for both the TOTAL and TREND cases and decrease in the DETREND cases as expected. In the

62

WH, however, there is no significant change when the criteria is applied.

In summary, there appears to be evidence in the average six-month spatial correlations that suggest high negative correlation between MSU channel 3 brightness temperature and mid-level geopotential height analyses for shorter, synoptic-scale patterns. This is particularly true in the WH and when the TOTAL channel 3 MSU 400-100-mb thickness correlation is high as well. Conversely, although the results are less clear, the 50-mb heights tend to be positively correlated with the larger -scale MSU patterns.

4. MSU and 500 mb Vorticity and Dynamic Tropopause

The 500-mb vorticity field has traditionally been an important analysis product in the forecasting of baroclinic waves and surface cyclones (e.g., Petterssen, 1956). A new analysis product, which is perhaps even more dynamically revealing in light of the theoretical rigor of PV thinking (Hoskins et al., 1985) is the dynamic tropopause analysis (e.g., Hoskins and Berrisford, 1988). Specifically, positive (negative) PV anomalies along isentropic surfaces near the tropopause correspond to low-cold (high-warm) dynamic tropopauses.

In the context of this study, Hirschberg and Fritsch (1991b) show that positive (negative) PV anomalies and the corresponding spatial characteristics of the tropopause are consistent with the presence of warm (cold) anomalies in the upper-troposphere and lower-stratosphere. Therefore, the channel 3 MSU pattern should show correspondence to the tropopause pattern as well. Furthermore, the hydrostatic and LID arguments presented in the previous section, suggests that

63

the MSU thermal patterns should also be related to the 500-mb vorticity field.

The six-month-average correlations between the MSU and 500-mb vorticity and the MSU and the dynamic tropopause analyses are presented in Tables 8 and 9, respectively. Both sets of correlations are consistent as expected since the 500-mb vorticity pattern is in reality an out-of-focus reflection of the tropopause-level PV distribution (Hoskins et al., 1985) All sub-domains show weak correlations between the TOTAL MSU and vorticity and tropopause analyses except for the Eastern Pacific (Area 5). Here the AT and TCC ≥ 0.80 correlations are ≥ 0.65. Interestingly, the EH and WH total correlations tend to be opposite signed. However, as with the 500-mb height correlations, there appears to be a scale dependency in the relationship between the MSU and the 500-mb vorticity and tropopause patterns. While the large-scale TREND correlations tend to reflect those for the TOTAL, the small-scale DETREND correlations exhibit a definite positive flavor especially for cases when the TCC ≥ 0.80 is applied. For these times the DETREND average across all sub-domains is 0.56. However, the Eastern Pacific (Area 5) exhibits no significant difference between TOTAL, DETREND and TREND analyses. Unfortunately, it is beyond the scope of this study to attempt a detailed explanation for this particular result. However, a possible reason might be the synoptic regime that dominated this portion of the world during the six-month period. In particular, occluded synoptic-scale disturbances present in the DETREND fields may tend to be more coupled with the large-scale disturbances present in both the TOTAL and the TREND fields. This is precisely the synoptic situation that occurs in the case study discussed in Chapter V.

AREA	TOTAL	DETREND	TREND
1. AT	-0.09	0.48	-0.38
TCC ≥0.80	-0.10	0.56	-0.41
TCC ⟨0.80	-0.42	0.34	-0.23
2. AT	-0.16	0.47	-0.41
TCC ≥0.80	-0.14	0.53	-0.40
TCC ⟨0.80	-0.30	0.00	-0.55
3. AT	-0.23	0.39	-0.42
TCC ≥0.80	-0.22	0.45	-0.43
TCC ⟨0.80	-0.27	0.36	-0.34
4. AT	0.06	0.56	-0.28
TCC ≥0.80	0.06	0.61	-0.27
TCC ⟨0.80	-0.02	0.43	-0.31
5. AT	0.65	0.59	0.59
TCC ≥0.80	0.68	0.63	0.45
TCC ⟨0.80	0.50	0.45	0.47
6. AT	0.44	0.54	0.34
TCC ≥0.80	0.48	0.57	0.39
TCC ⟨0.80	0.26	0.31	0.17
7. AT	0.33	0.55	0.14
TCC ≥0.80	0.44	0.58	0.23
TCC ⟨0.80	-0.10	0.39	-0.15
8. AT	0.34	0.51	0.14
TCC ≥0.80	0.43	0.58	0.24
TCC ⟨0.80	0.03	0.31	-0.13

Table 8. As in Table 4, except for MSU and 500-mb vorticity.

AREA	TOTAL	DETREND	TREND
1. AT	-0.01	0.47	-0.29
TCC ≥0.80	0.00	0.57	-0.30
TCC ⟨0.80	-0.05	0.32	-0.26
2. AT	-0.11	0.43	-0.37
TCC ≥0.80	-0.08	0.53	-0.35
TCC ⟨0.80	-0.32	0.33	-0.55
3. AT	-0.22	0.38	-0.45
TCC ≥0.80	-0.21	0.49	-0.44
TCC ⟨0.80	-0.32	0.32	-0.47
4. AT	0.04	0.55	-0.33
TCC ≥0.80	0.05	0.60	-0.33
TCC ⟨0.80	0.15	0.42	-0.43
5. AT	0.66	0.60	0.60
TCC ≥0.80	0.70	0.65	0.63
TCC ⟨0.80	0.47	0.42	0.45
6. AT	0.43	0.50	0.30
TCC ≥0.80	0.47	0.53	0.36
TCC ⟨0.80	0.23	0.26	0.11
7. AT	0.29	0.46	0.14
TCC ≥0.80	0.40	0.50	0.25
TCC ⟨0.80	-0.12	0.23	-0.17
8. AT	0.34	0.48	0.15
TCC ≥0.80	0.44	0.56	0.27
TCC ⟨0.80	-0.02	0.25	-0.16

Table 9. As in Table 4, except for MSU and Dynamic Tropopause.

5. MSU and Sea Level Pressure

Finally, we examine the spatial relationship between the channel 3 MSU and sea-level pressure analyses. Over the life cycle of a typical surface cyclone, the spatial relationship between features associated with the upper-level dynamics (i.e., upper-level PV anomalies, stratospheric warm pools etc.) and the surface low varies. In particular, Hirschberg and Fritsch's (1991b) conceptual model (Fig. 3) describes how the relationship between tropopause-level thermal anomalies and surface lows change during baroclinic development. During the initial stages of cyclogenesis, warm pools associated with the low portions of tropopause undulations are often found upstream of the nascent surface low. As development proceeds, this phase lag decreases until occlusion when the warm anomaly and surface low are vertically stacked. Consequently, as Velden (1992) has qualitatively demonstrated, the channel 3 MSU pattern (which is indicative of the spatial configuration of the tropopause-level thermal anomalies), should exhibit various phase relationships and hence correlations with the sea-level pressure analysis depending on the stage of cyclogenesis. Over a long temporal period, which exhibits migrant baroclinic-wave activity we should therefore expect the correlations to be low.

The average six-month spatial correlations (Table 10) bear this out. Generally poor negative correlations exist for all scales. Specifically, the average coefficient over the TOTAL, TREND and DETREND TCC $\geq$ 0.80 is only -0.34. An exception to this low correlation is over Area 5 (northeastern Pacific) where the TOTAL correlation jumps to -0.75. This high correlation is possibly a reflection of the Aleutian low system. More will be said about this when the temporal corrrelation results are discussed in the next section.

67

AREA	TOTAL	DETREND	TREND
1. AT	-0.29	-0.21	-0.18
TCC ≥ 0.80	-0.30	-0.30	-0.19
TCC < 0.80	-0.24	-0.06	-0.16
2. AT	-0.28	-0.08	-0.26
TCC ≥ 0.80	-0.28	-0.20	-0.27
TCC < 0.80	-0.26	0.03	-0.13
3. AT	-0.09	-0.11	-0.10
TCC ≥ 0.80	-0.10	-0.17	-0.11
TCC < 0.80	-0.09	-0.08	0.21
4. AT	-0.42	-0.32	-0.48
TCC ≥ 0.80	-0.41	-0.36	-0.49
TCC < 0.80	-0.49	-0.24	-0.27
5. AT	-0.74	-0.70	-0.65
TCC ≥ 0.80	-0.75	-0.73	-0.66
TCC < 0.80	-0.65	-0.60	-0.60
6. AT	-0.25	-0.31	-0.20
TCC ≥ 0.80	-0.26	-0.32	-0.22
TCC < 0.80	-0.21	-0.22	-0.13
7. AT	-0.23	-0.27	-0.12
TCC ≥ 0.80	-0.32	-0.29	-0.18
TCC < 0.80	0.10	-0.14	0.06
8. AT	-0.34	-0.39	-0.19
TCC ≥ 0.80	-0.43	-0.47	-0.29
TCC < 0.80	-0.01	-0.16	0.07

Table 10. As in Table 4, except for MSU channel 3 and sea-level pressure.

B. TEMPORAL CORRELATIONS

The temporal correlations between the 12-hourly channel 3 MSU brightness temperatures and the 400 - 100 mb thickness, 500-mb height, 50-mb height, 500-mb vorticity, 200-mb temperature, dynamic tropopause, and sea-level pressure over the six-month study period are presented in this section. Although there should be redundancies in the spatial and temporal statistics, each set of results can provide insights that the other set does not. For example, analyses of the grid-point temporal correlation coefficients enable more detailed insights as to how the MSU compares to the conventional analyses over the study domain. In the following, three sets of temporal correlation analyses will be discussed for each MSU-conventional comparison: 1) unfiltered (UF), 5 day high-pass filtered (HP) and , 14 day low-pass filtered (LP). Like the AT, DETREND, and TREND spatial categorizations, these analyses correspond to the full spectrum, the short (≤synoptic)-scale and the long-wave portions, respectively, in the temporal data.

1. MSU and 400 - 100 mb Thickness

The MSU channel 3 brightness temperature and 400 - 100-mb thickness temporal correlations over the six-month period show generally high positive coefficients over the entire global domain and for all wavelengths (Fig. 14). This result is not surprising in light of the fact that the channel 3 MSU weighting function is designed to sense the microwave energy primarily originating between the 400 and 100-mb pressure surfaces. It is also consistent with the high positive six-month average spatial correlation findings of the previous section. In particular, the UF analysis (Fig. 14a) exhibits
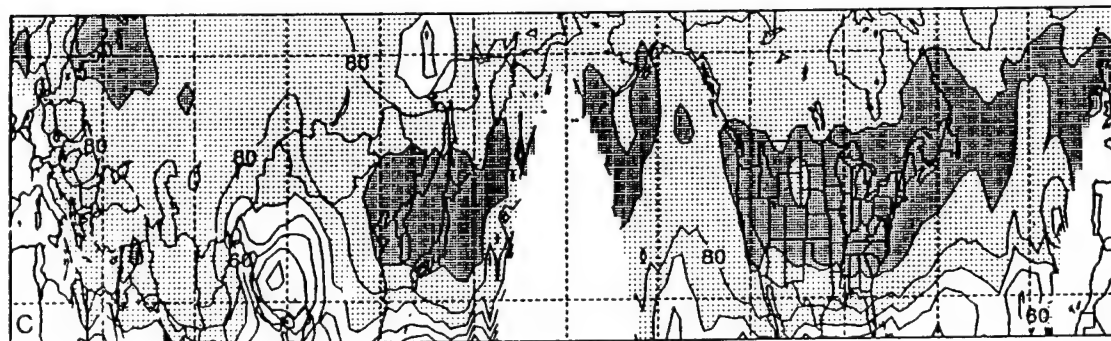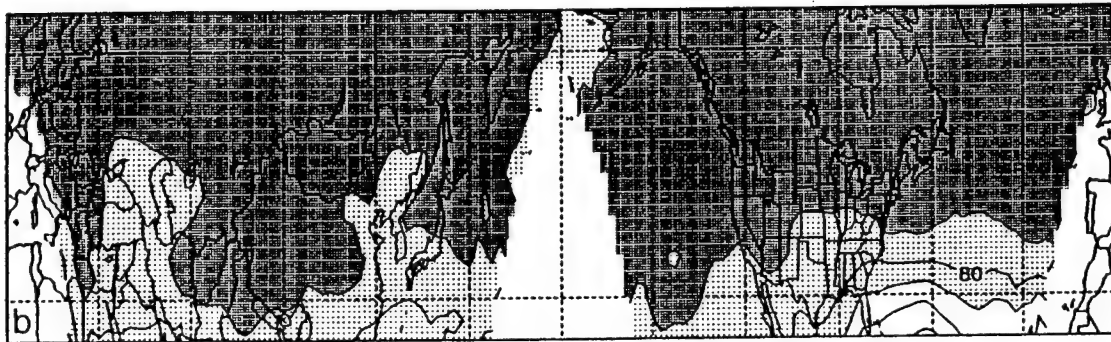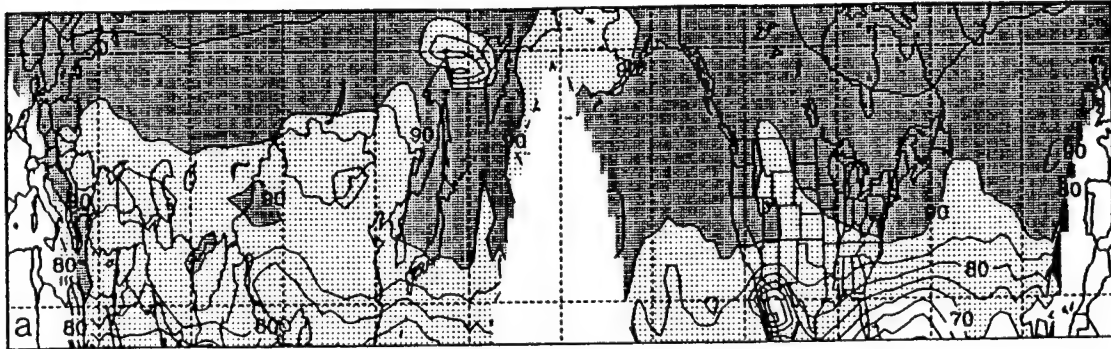
69

Figure 14. Analysis of (a) unfiltered (UF), (b) 14 day low-pass filtered (LF), and (c) ≤ 5 day high-pass filtered (HF) six-month temporal correlation coefficients (solid, contour interval 10^{-2}) between the channel 3 MSU and 400–100-mb thickness. Light (dark) stippling represents correlations ≥ 0.70 (≥ 0.90).

no correlation < 0.70 while half the domain shows coefficients of 0.90 or better. The LP analysis (Fig. 14b) suggests even stronger positive correlation between the long-wavelength portion of the MSU-400-100-mb thickness signal.

Similarly, the HP analysis (Fig. 14c) shows generally high positive temporal correlation between the MSU and 400-100-mb thickness fields. This analysis is interesting for a number of reasons. Whereas the UF (Fig. 14a) and LP (Fig. 14b) analyses exhibit increases in the positive correlations toward higher latitudes, the HP analysis (Fig. 14c) shows a general decrease. Strikingly, at the shorter time-scales captured by the HP analysis, the sense of the climatological "storm track" is evident as correlation bands of higher than 0.90 generally tend northeastward from east Asia to the Aleutians and from the western U.S. to the northwestern Atlantic. There is also a clear center of poor correlation across the Tibetan Plateau near 90° E. This indicates that the channel 3 MSU is either contaminated by high-topography surface emission at synoptic-scale wavelengths or NMC GDAS analyses are poorer in this area. Since the MSU senses microwave energy at mid-levels of the atmosphere (~400 mb), it can potentially be contaminated over regions that contain topography (e.g., the Himalayas) that reaches the mid levels of the atmosphere. The anomalous area of poor correlations over northeast Siberia (Fig. 14c) may be attributed to contamination by snow cover. More will be said about this possibility in Section C.

One of the goals of this study was to ascertain whether a conventional data-rich-regions versus data-poor-regions (e.g., sea-land) contrast would exist in the correlations between the MSU and conventional analyses. It was speculated that the correlations would drop over conventional data-poor regions particularly upstream of radiosonde networks. There is some hint of this in the HP MSU-400-100-mb thickness

71

correlation results (Fig. 14c) over the Northeastern Pacific. However, it appears that the correlations are more dependent on the climatological storm-track than any influence of poorer oceanic analysis. Perhaps this suggests that the analysis over data-sparse regions are influenced more by satellite data than previously thought.

2. MSU and 200 mb Temperature

As expected, the temporal correlation analyses of MSU and 200-mb temperature (Fig. 15) also indicate relatively high positive correlation over much of the global domain. When the data is high-pass filtered to remove the wavelengths with periods > 5 days (Fig. 15c), high positive correlations (> 0.80) are found over eastern Asia and the WH. This finding is in general agreement with the spatial correlation results and also the findings of Velden (1992), who qualitatively demonstrated the correlation between warm anomalies in the MSU channel 3 brightness temperature and upper-level temperature analyses during selected cyclone cases. Unlike Velden's findings, however, the six-month results suggest that the strongest positive correlations between the MSU and a single isobaric temperature analysis lie at 200 mb rather than at 250 mb (not shown). Significantly, the high positive correlations found here in the six-month data set suggest that the MSU channel 3 brightness temperature analyses can be utilized to track synoptic-scale tropopause-level thermal anomalies with a high degree of confidence.
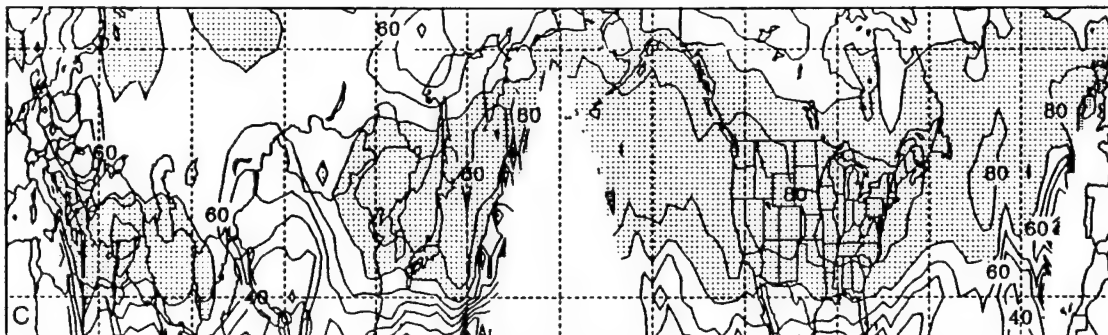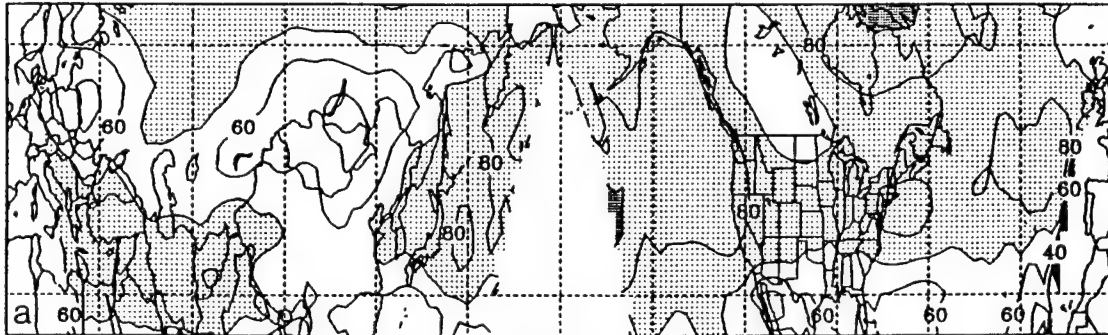
72

Figure 15. As in Fig. 14 except for channel 3 MSU and 200-mb temperature correlations.

3. MSU and 500 mb Height and 50 mb Height

Comparison of the channel 3 MSU 50-mb height and MSU 500-mb height temporal correlations (cf. Figs. 16 and 17) provides further evidence for the thickness spreading argument discussed in Section A.3 and the forecasting utility of the MSU analyses. Specifically, the UF (Fig. 16a) and to an even greater extent, the LP (Fig. 16b) analyses show relatively high positive correlations between the MSU and the 50-mb heights over most of the domain. Conversely, relatively little correlation is evident between the MSU and the 500-mb heights in the UF (Fig. 17a) and LF (Fig. 17b) analyses. An exception to these results is over the central and eastern north Pacific where relatively high negative correlations (< - 0.70) are found in the UF and LF charts (Figs. 17a,b). Such relatively high negative correlations were also found in the spatial results (Table 6) and are possibly attributable to the strong semi-permanent long-wave trough that persisted over the six month study period. In any event, aside from this area, the UF and LF temporal analyses generally suggest that large-scale thermal anomalies are spread upwards. That is, long wavelength thermal anomalies tend to affect the geopotential heights above them. Although the spatial results are consistent with this conclusion over the EH, it is unclear in light of these temporal findings, why they are not consistent over the WH. Recall that the AT and TREND MSU-50-mb height spatial correlations (Table 7) over the WH are low. This discrepancy is especially troublesome since the spatial and temporal correlations for the other parameters of interest appear consistent.

It is important to note that, when the synoptic-scale wavelength ($\leq$ 5 day period) signals in the six-month MSU and 50-mb heights are compared, the correlations (Fig. 16c) across the whole domain decrease.

74

Figure 16. As in Fig. 14 except for channel 3 MSU and 500-mb height correlations. In regions of negative correlations, contour intervals are dashed and light stippling represents correlations ≤ 0.70.
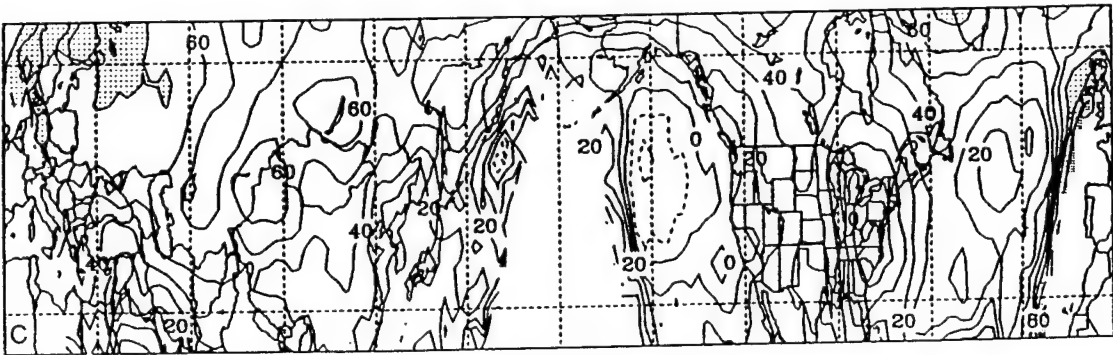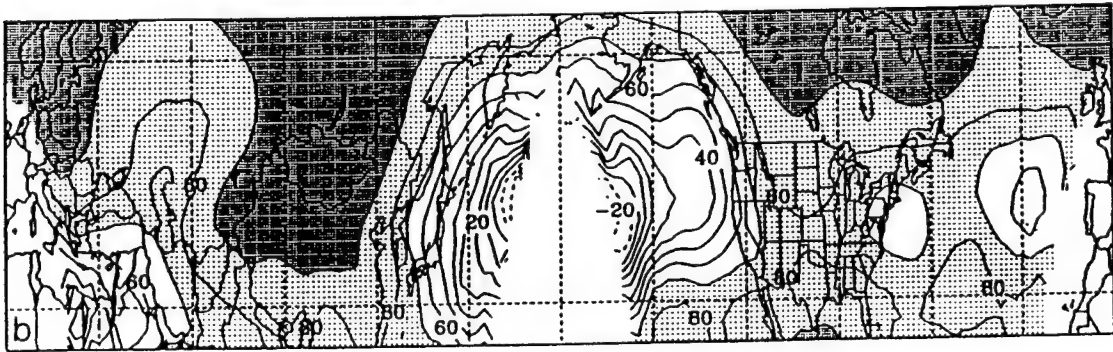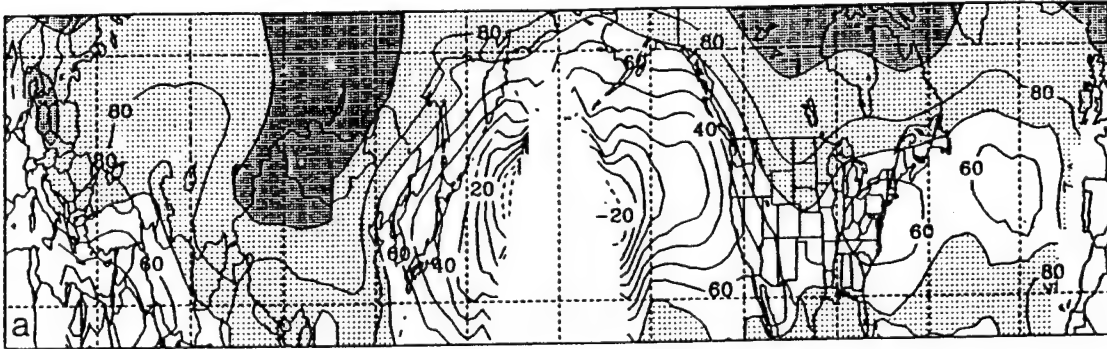
75

Figure 17.   As in Fig. 14 except for channel 3 MSU and 50-mb height correlations.

However, high negative correlation (≤ -0.70) between the MSU and the 500-mb heights (Fig. 17c) becomes dominant aside from the notable exception over the Tibetan Plateau. A region of negative correlations ≤ -0.80 from eastern Asia to the northwestern Atlantic again outline the sense of the favored synoptic-scale storm tracks. Similar to the DETREND spatial correlations, these HP results indicate that small-scale thermal anomalies are spread downwards. In terms of the potential forecasting application, warm (cold) anomalies in the channel 3 MSU appear to correspond well with small-scale (≤ synoptic scale) trough (ridge) features in the 500-mb height pattern.

4. MSU and 500 mb Vorticity and Dynamic Tropopause

Similar to the spatial results, the channel 3 MSU 500-mb vorticity and MSU-dynamic tropopause temporal correlations are consistent with one another (cf. Figs 18 and 19) and with the height field comparisons. The UF and LF analyses show generally low positive correlations between the MSU and the 500-mb vorticity (Figs. 18a, b) and the dynamic tropopause (Figs. 19a, b) although an area of relatively high positive correlation appears again over the central and northwestern Pacific ocean. Consistent with the scale dependance hypothesis, a pattern of higher positive correlations emerge, especially in the MSU-dynamic tropopause analysis (Fig. 19c), after the data has been put through the 5 day high-pass filter to exclude longer than synoptic-scale disturbances. In particular, > 0.70 correlations are evident across the storm tracks from eastern Asia to the northwestern Atlantic.
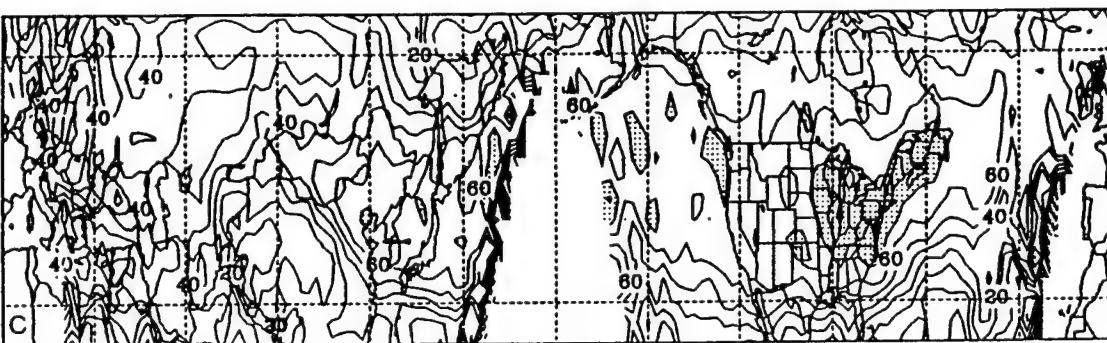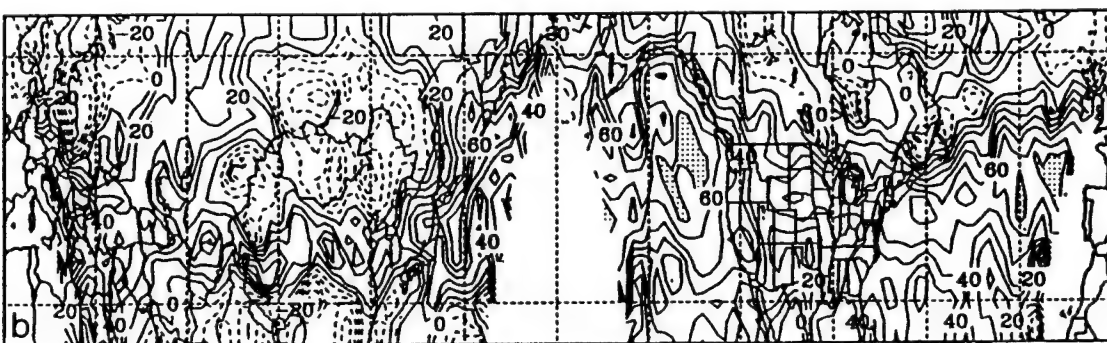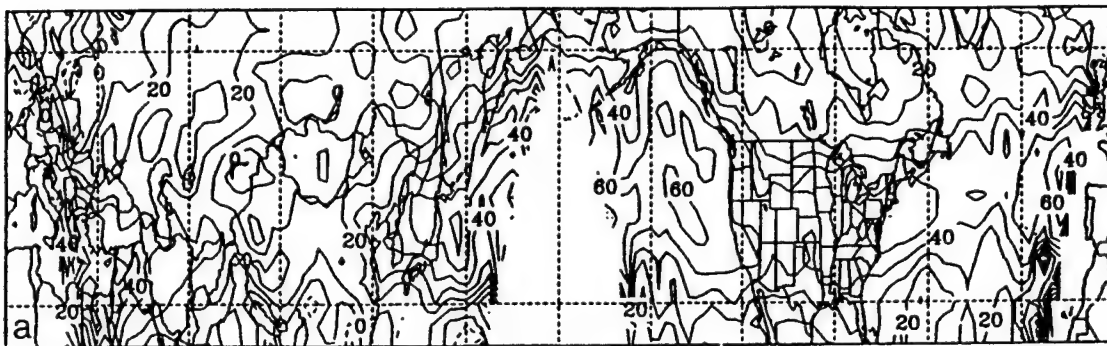
Figure 18. As in Fig. 14 except for channel 3 MSU and 500-mb vorticity correlations.
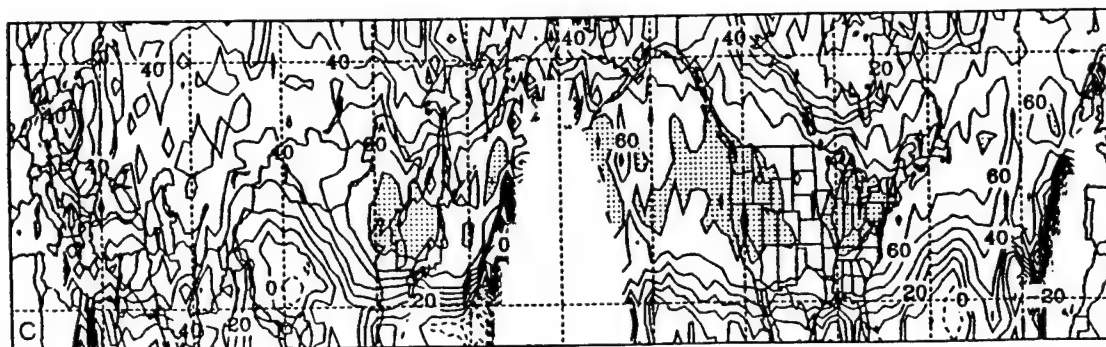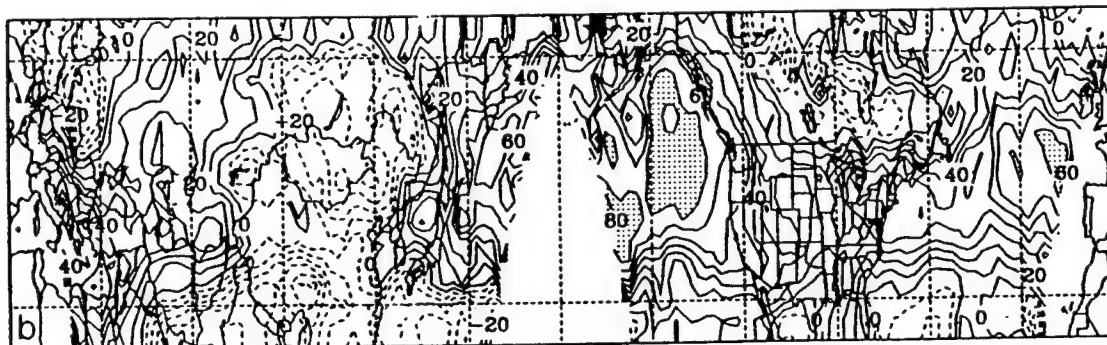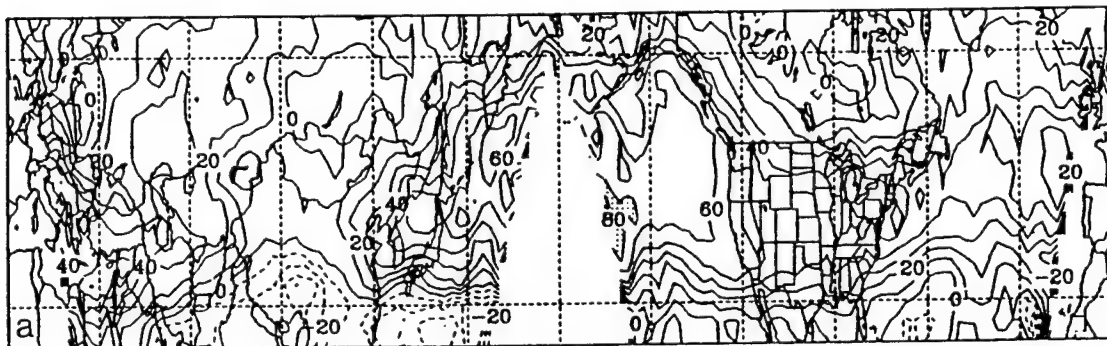
78

Figure 19. As Fig. 14 except for channel 3 MSU and dynamic tropopause correlations.

5. MSU and Sea Level Pressure

Finally, the temporal correlation analyses between the channel 3 MSU and sea-level pressure show characteristics similar to those deduced from the analogous spatial comparison. The UF and LF analyses (Figs. 20a,b) generally indicate poor negative correlation between the MSU and sea level pressure except in three areas: northeast of Japan, the northeastern Pacific, and the central north Atlantic. Correlations in these areas are generally better than -0.70. Again, these high correlations probably reflect the existence of the "semi-permanent" long-wave trough and ridge systems (Holton, 1979) and the associated low and high mean sea-level pressures, respectively. In particular, these areas would be expected to have relatively warm (in the case of troughs) and cold (in the case of ridges) mean channel 3 MSU brightness temperature signatures.

The 5 day HP analysis (Fig. 20c) of MSU and sea-level pressure correlation exhibits decreased negative correlations in comparison to the lower frequency comparison. As with the spatial correlation results, this general lack of temporal correlation between the MSU channel 3 brightness temperatures and sea-level pressure over most of the domain is indicative of the phasing sequence that occurs between tropopause-level anomalies and surface pressure systems during the life cycles of baroclinic waves. For example, only during occlusion should the warm channel 3 MSU brightness temperature anomalies become coincident with surface lows. Support for this hypothesis is found in the HP analyses over the areas south of the Kamchatka Peninsula and the Gulf of Alaska. These locations, known to the "grave yard" of deep, vertically stacked occluded lows, exhibit fairly high negative correlations.
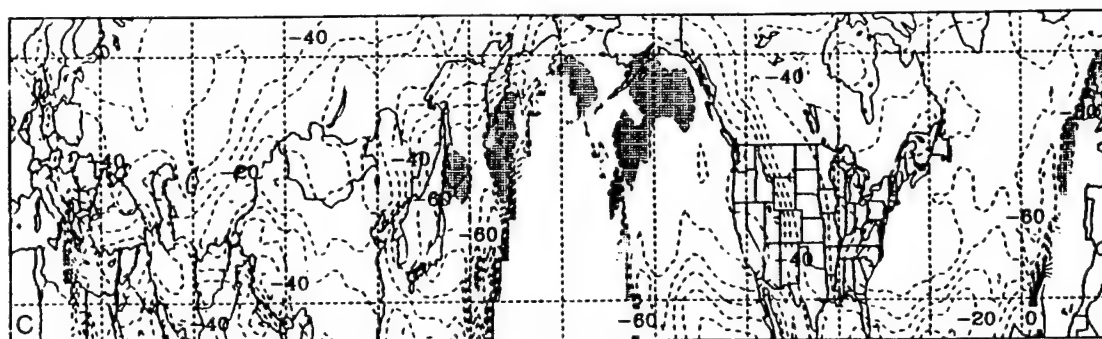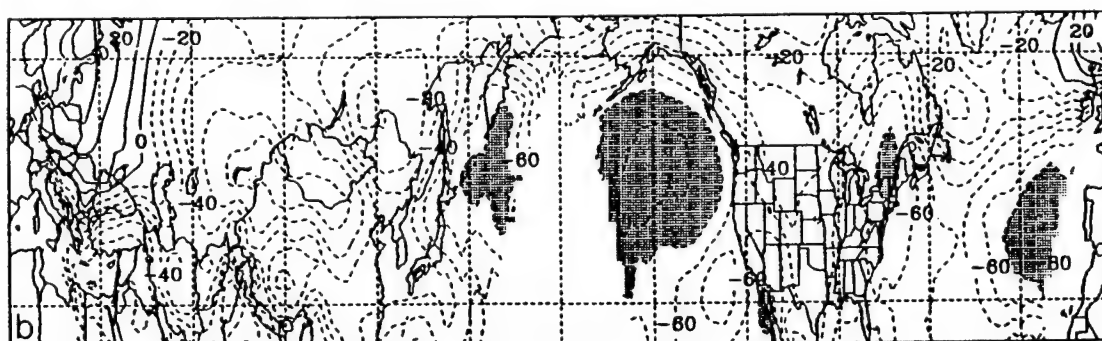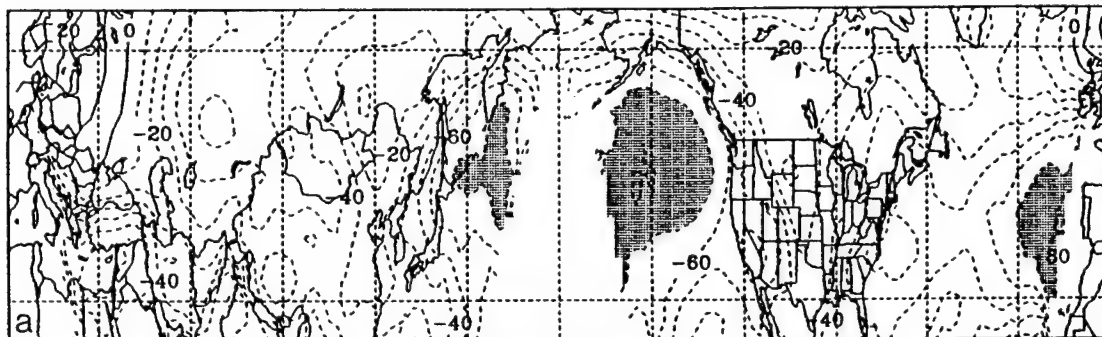
Figure 20. As in Fig. 16 except for channel 3 MSU and sea-level pressure correlations.

C. SOURCES OF ERRORS

The results of this six-month statistical comparison between the channel 3 MSU brightness temperature data and the conventional fields certainly suggest the utility of the MSU as a nowcasting and forecasting tool for baroclinic waves. To be complete, sources of error, not only in this study, but also in any potential operational application should be considered.

Probably the most clearly identifiable problem is the contamination of the channel 3 MSU information by surface emission. This is especially an issue over locations with relatively high topographic features such as the Tibetan Plateau. Another possible source of surface contamination is over broad expanses of snow-covered terrain such as that found over most of northern Asia during the winter. Apparently, this surface contamination owing to high surface emissivity, can be compounded by coupling the channel 3 MSU brightness temperature data with lower channels (channels 1 and 2) of the MSU because of the development of statistical limb correction coefficients (Spencer, 1992). As mentioned above, surface contamination of the channel 3 MSU brightness temperatures is a possible reason for the lower than expected spatial and temporal correlations found in the comparison of the MSU with conventional fields over Asia.

Other data-related error sources include instrument error in the MSU itself and residual limb darkening effects not completely corrected. There may also be errors in the data analysis procedure. In particular, phase errors certainly occur owing to the inclusion of MSU data over the 3-h time window. In addition, errors may also arise from the objective analysis technique utilized to construct both the MSU brightness-temperature and the conventionally-derived fields.

The high correlation results though suggest these errors are generally small and do not adversely impact the spatial and temporal correlations.

V. LOCAL COLLECTION AND PROCESSING OF MSU DATA

One potential use of the MSU brightness temperature data is to locally collect and process it as the NOAA polar orbiters pass overhead. Based on the dynamic and statistical relationships found in the six-month data set, the resulting local MSU analyses could then be evaluated in real time to aid in the nowcasting and forecasting of important baroclinic features in the vicinity. To demonstrate the feasibility of such a procedure, MSU brightness temperature data were collected and processed in real time for a portion of the 1994 cold season (1 January - 31 March 1994) at the Naval Postgraduate School. In this chapter, a description of the local MSU collection and processing is described. In addition, an individual case study illustrating the usefulness of the local MSU analyses is presented.

A. LOCAL DATA ANALYSIS AND PROCESSING

The locally-collected MSU data is automatically post-processed and archived to tape immediately after capture. The local collection and data processing system consists of a 1.5-m S-band parabolic satellite dish with associated power drive, a Telonics HRPT receiver, and various Silcon Graphics and Sun workstations. The satellite dish is roof-mounted and provides longitudinal coverage from the mid-U.S. westward to the Central Pacific (~ 100^0 W to 140^0 W) and latitudinal coverage from approximately 20^0 N and 60^0 N. Coordinates for driving the satellite dish for interception of the NOAA TIROS-N High Resolution Picture Transmission (HRPT) signal generated by the NOAA TIROS-N satellites is determined from the satellite-dependent ephemeris data updated weekly. The ephemeris data is input automatically into the Telonics HRPT

receiver as it is received and new "windows" for collection of data are generated.

The post processing includes a mix of routines within the larger processing framework of Terrascan, a software package commercially available from SeaSpace Corporation. The initial post processing of the MSU data (Fig. 21) includes standard routines to download, decommutate and earth-locate the data, with follow on satellite-dependent calibration. The calibrated data is then corrected for surface emissivity, antenna side lobes and limb effects. The limb correction is based on statistical regression coefficients that correct the non-nadir footprints to nadir. This procedure is discussed in further detail in Chapter III. Brightness temperatures are computed using equation (14). The brightness temperatures corresponding to a particular map time are then segregated by satellite. A multiquadric interpolation scheme (Nuss and Titley, 1994) is used to objectively analyze the data on a 100 km (75 x 59 grid points) Lambert conformal map centered near 40^0 N, 120^0 W. An average of five passes are processed per 24-h period.

B. CASE STUDY

Finally, a individual case study is described to illustrate the utilization of a local MSU analysis. The event encompassed a 36-hr period from 1200 UTC 23 to 0000 UTC 25 January 1994 (hereafter denoted as 25/0000) and was highlighted by a developing short-wave trough in the Eastern Pacific (EP) that reinforced an occluded cyclone system in the southeastern Gulf of Alaska (GA). In this example, the focus will be on the synoptic evolution of the 300-mb height, 300-mb
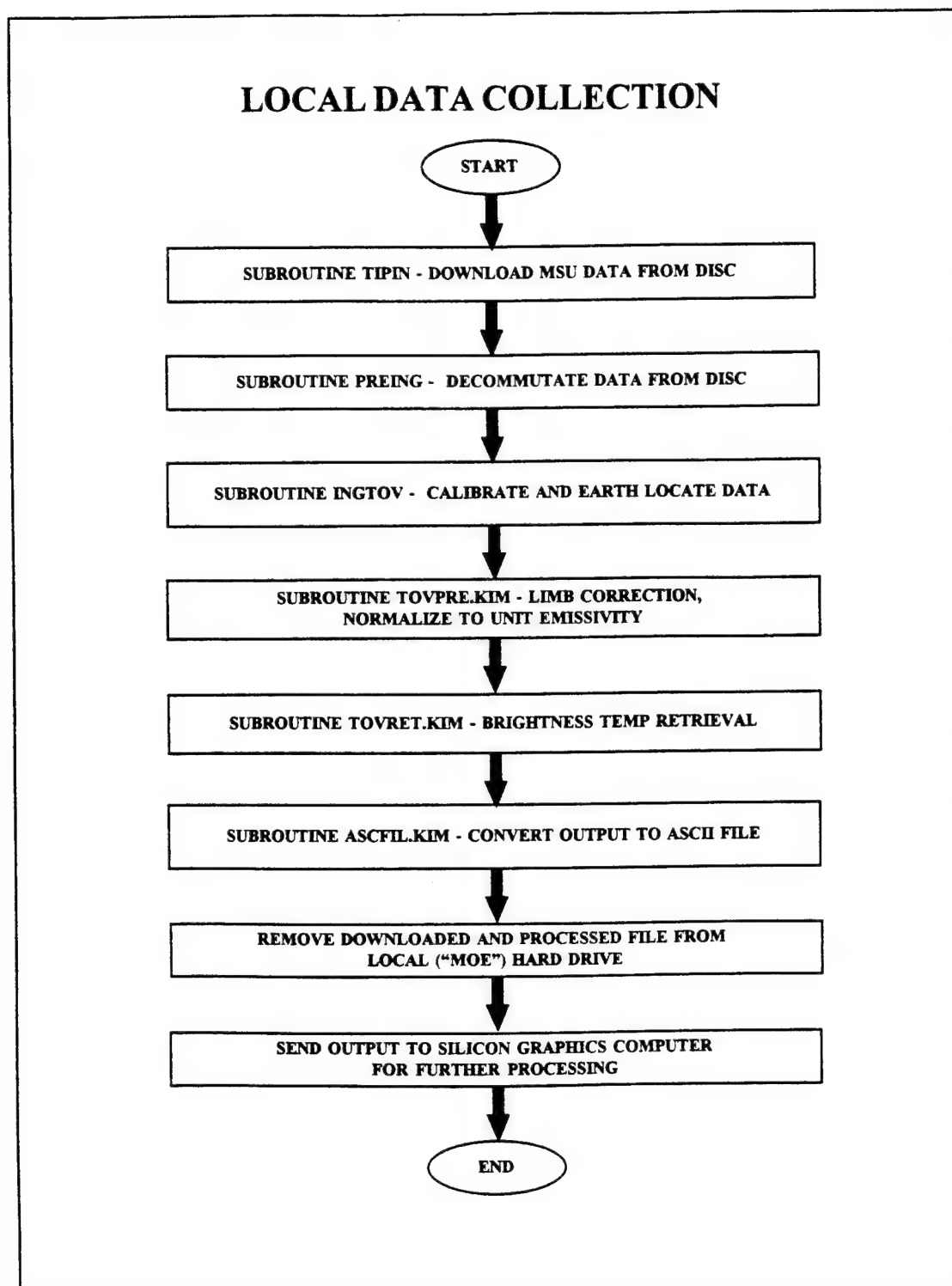
86

Figure 21. Flowchart depicting the post-processing of MSU data during the local collection phase of the study.

potential vorticity (PV), 200-mb temperature, and the channel 3 MSU brightness temperature patterns.

The 23/1200 Navy Operational Global Atmospheric Prediction System (NOGAPS) 300-mb height and PV analysis (Fig. 22a) shows the presence of a deep upper-level trough centered near 50° N, 140° W. A 988-mb cyclone (not shown) is located near this position at sea level. Multiple embedded PV centers can be seen rotating around the trough. The main PV center (> 7.0 PV units) was located just to the west of the base of the trough. This positive PV anomaly was associated with a short-wave trough and jet streak feature that had moved southeast out of the GA prior to this time. A 200-mb (Fig. 22b) warm anomaly (> -48° C) generally correlates well with the 300-mb trough position. The channel 3 MSU analysis valid at 23/1337 (Fig. 22c) shows a similar warm anomaly (> -46° C). At this map time, statistically significant correlation coefficients of $\rho_{PV} = = 0.80$ and $\rho_{T200} = 0.86$ are obtained between the channel 3 MSU analysis and the 300-mb PV analysis, and the channel 3 MSU analysis and the 200-mb temperature analysis, respectively. Although this particular satellite pass does not provide enough areal coverage to determine if the MSU anomaly was closed, a later off-synoptic-time pass valid at 23/1732 (not shown) indicates a closed, intensifying anomaly that is progressing southeastward.

Over the next 12-h, the upper-level trough progressed slightly southeastward. By 24/0000 the NOGAPS 300-mb height and PV analysis (Fig. 22d) shows a kidney-shaped positive PV anomaly near the center of the trough with maximum value of > 6.0 PV units. The southwestern portion of this anomaly was associated with the short-wave trough and jet streak feature that was now approaching the base of the long-wave trough. The 200-mb (Fig. 22e) warm anomaly (> -48° C) generally remains over the 300-mb trough and positive PV anomaly positions. The channel 3 MSU analysis valid at 24/0102

88

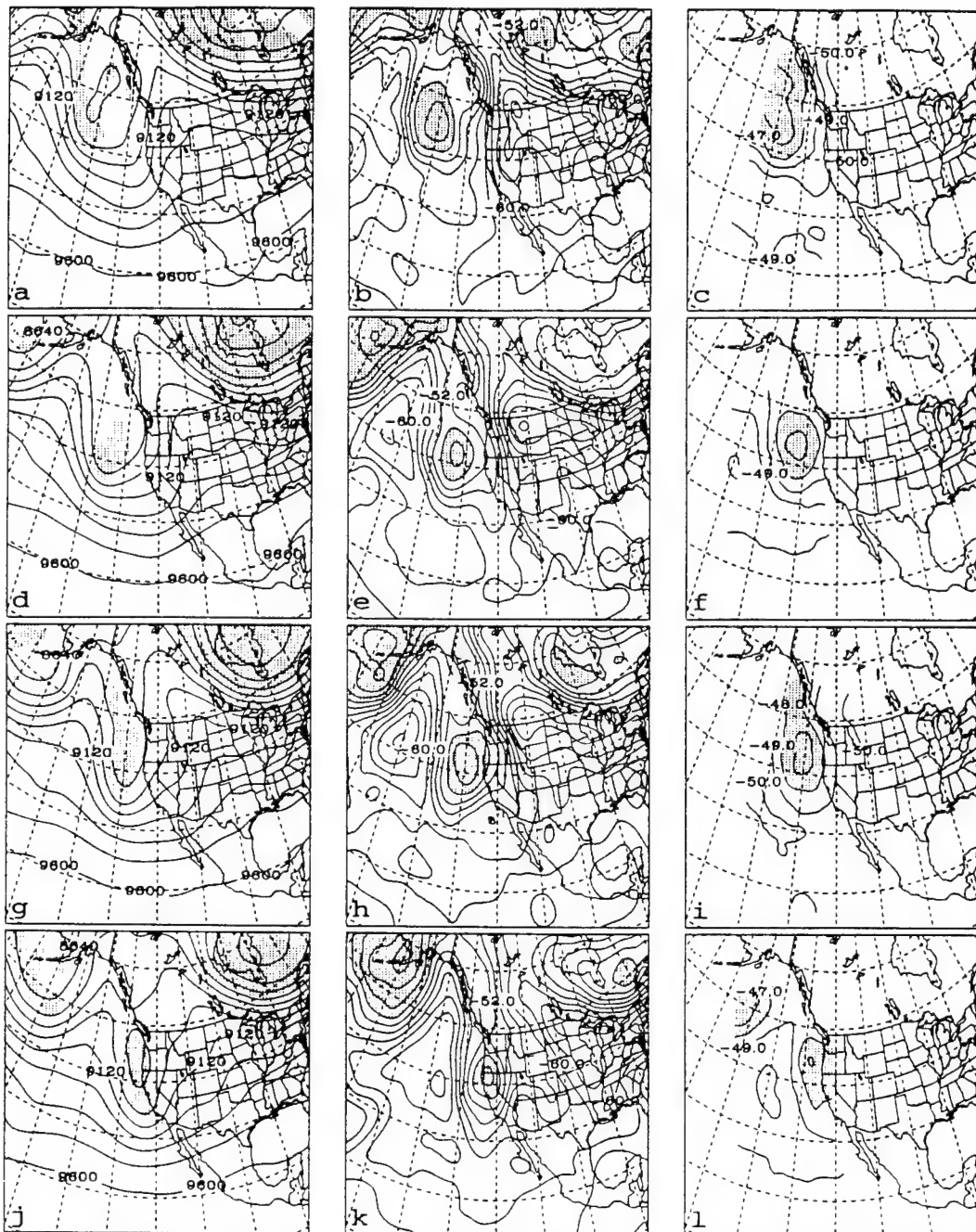**Figure 22.** Horizontal analyses of 300-mb height (solid, contour interval 120 m) and PV (values > 5.0 PV units dot filled)[a,d,g,j]; 200-mb temperature (contour interval 2^0C)[b,e,h,k]; and channel 3 MSU brightness temperature (contour interval 1^0C)[c,f,i,l] for 23/1200, 24/0000, 24/1200, and 25/0000, respectively. Lower left latitude-longitude value is 10^0 N, 150^0 W. Latitude-longitude increment is 10^0.

(Fig. 22f) shows a similarly shaped warm anomaly ($> -46°$ C). Again, relatively high statistically significant correlation coefficients of $\rho_{PV} = 0.79$ and $\rho_{T200} = 0.87$ are obtained at this time.

After 24/0000, the 300-mb trough sharpened and drifted eastward as the short-wave trough continued its migration through the base of the long-wave trough (Fig. 22g). Although the 300-mb positive PV anomaly increased in value (> 9.0 PV units) both the value of the 200-mb anomaly (Fig. 22h) and the channel 3 MSU (Fig. 22i) warm anomalies did not change appreciably although the areas of each expanded somewhat. Significantly, the MSU anomaly remained spatially well correlated with the conventional analyses. Statistically significant correlation coefficients of $\rho_{PV} = 0.86$ and $\rho_{T200} = 0.84$ are obtained at this time. In addition, note that the MSU analysis appears to depict the sharpness of the 300-mb trough and PV structure better than the 200-mb thermal analysis.

Finally, by 25/0000 the NOGAPS analysis (Fig. 22j) shows the 300-mb trough closing off and beginning to cross the coast. The trough axis was now negatively tilted (NW – SE) as the short-wave feature had migrated slightly downstream of the long-wave trough axis. Associated with this progression of the trough axis was a slight weakening and elongation of the PV anomaly. Oddly, the 200-mb analysis (Fig. 22k) now shows the warm anomaly downstream of the 300-mb trough/PV feature. Over the previous 12 hr, this warm anomaly maintained intensity, but decreased in size. The 25/0050 MSU analysis (Fig. 22l) indicates the warm anomaly weakening but remaining offshore in a manner more consistent with the 300-mb pattern. This analysis also suggests an elongation in the pattern. At this time, the statistically-significant correlation coefficients are $\rho_{PV} = 0.70$ and $\rho_{T200} = 0.88$.

The strong spatial correlations of the channel 3 MSU brightness temperature pattern with the 200-mb thermal and 300-mb PV patterns at each map time in Figure 22 is confirmed in the 36-h time-averaged statistics presented in Table 11. Specifically, statistically-significant spatial correlation coefficients of $\rho_{T200} = 0.87$ and $\rho_{PV} = 0.79$ are found over the duration of this cyclone event. Table 11 also presents correlations of channel 3 MSU brightness temperature patterns with a number of other conventional fields. In particular, note the high correlation between the channel 3 MSU and sea-level pressure ($\rho_{slp} = -0.81$). This MSU-sea-level-pressure correlation for the 36-h time period is much higher than the average Eastern Pacific 5 day high-pass filtered correlation found in the six-month dataset. This can be explained by the fact that this individual 36-h case involved a well-developed occluded cyclone that was vertically stacked. Thus, the warm temperature anomaly at 200-mb remained generally over the surface cyclone throughout the period. As discussed in Chapter IV, immature systems such as those studied by Velden (1992), that are tilted in a sense that favors baroclinic development, would not exhibit such high correlations between the MSU channel 3 and sea-level pressure.

91

Field	Correlation ρ
1. Sea-level pressure	−0.81
2. 1000 − 500 mb thickness	0.46
3. 250-mb temperature	0.49
4. 200-mb temperature	0.87
5. 500-mb height	−0.62
6. 200-mb height	−0.47
7. 500-mb vorticity	0.63
8. 300-mb pot. vorticity	0.79

Table 11. Time-averaged correlation coefficients between channel 3 MSU brightness temperatures and conventionally derived fields over the 36-h period 1200 UTC 23 − 0000 UTC 25 January 1994.

VI. CONCLUSIONS AND RECOMMENDATIONS

In this thesis, a six-month climatological study was undertaken to quantitatively determine the potential usefulness of channel 3 MSU brightness temperature data as a nowcasting and forecasting tool. Specifically, both area-average and point-wise temporal correlations between the NOAA polar-orbiter MSU and various conventionally-derived fields were calculated over the Northern Hemisphere mid-latitudes from 1 October 1993 - 31 March 1994.

In general, statistically-relevant correlations were found between the MSU and various conventional fields that have been shown to be dynamically linked to the upper-level temperature field and baroclinic wave development. As expected, the strongest positive correlations existed between the channel 3 MSU and the 400-100-mb thickness field. In particular, high positive correlations ($\rho_{thick} \geq 0.80$) between these two fields were evident in both time and space and over all wavelength and periods in the global data. Thus, features in the 400 - 100 mb thickness are readily observed by the channel 3 MSU over the majority of the global domain and can be used with a high degree of confidence for tracking these features.

Another measure of the potential usefulness of the channel 3 MSU is to detect and track more specific thermal anomalies along the tropopause. These tropopause-level thermal anomalies have been shown by Hirschberg and Fritsch (1991a,b) and others to be important features in cyclogenesis. The ability of the channel 3 MSU to detect and track these features is evident in the high positive temporal correlations ($\rho_{T200} \geq 0.80$) found between the full spectrum of MSU and the 200-mb temperature patterns over much of the domain. These 200-mb temperature correlations are consistent with what

93

Velden (1992) found in his qualitative study although he found the best correlations to occur at 250 mb rather than at 200 mb.

Significantly, the six-month results provide evidence for the LID hypothesis and the consequent thickness-spreading argument posed by Hirschberg and Fritsch (1993b). In particular, generally high positive correlations were found between the MSU and the 50-mb heights for wavelengths and periods greater than synoptic scale. This indicates that upper-level thermal anomalies are hydrostatically spread upwards in the height field on these scales. Conversely, relatively high negative correlations were found between the MSU and the 500-mb heights on scales less than or equal to synoptic. This indicates that smaller-scale thermal anomalies are spread downwards in the height field. Specifically, correlations $\rho_{H500} \leq -0.80$ between the short-wavelength, high frequency MSU-500-mb heights were found over much of the mid-latitudes. An exception to this was across western and central Asia where possibly the channel 3 MSU is contaminated by surface emission or there are errors in the NMC GDAS analyses. In addition, there were some differences between the large-scale MSU-50-mb height spatial and temporal correlations over the Western Hemisphere. While the temporal results showed the expected high positive correlation, the spatial results displayed low correlation. The reasons for this discrepancy remain an issue for further research. Nevertheless, despite these discrepancies, the channel 3 MSU indicates a high degree of reliability for tracking synoptic-scale mid-level waves that are traditionally associated with cyclogenesis.

Important insights are also obtained from the results of the correlation between the channel 3 MSU brightness temperature and the fields of mid-level vorticity and upper-level PV, the latter of which is often embodied in the

analysis of the dynamic tropopause. Again, for the synoptic-scale signals, correlations of better than 0.70 were generally found over the climatological "storm track" regions of the world. This linkage between the channel 3 MSU and these important dynamical fields provides evidence that the MSU is potentially useful in detecting and tracking important atmospheric phenomena associated with cyclogenesis especially at off-synoptic times and over data sparse regions.

The channel-3 MSU was found to be less useful in locating synoptic-scale sea-level pressure features. This expected finding is due to the phasing sequence that occurs between upper-level thermal anomalies and low-level cyclones during development.

Finally, a local MSU-collection and -processing procedure, performed with commercially available equipment and software, was described. The feasibility and usefullness of real-time, locally-generated MSU analyses as forecast aids was demostrated by reviewing an individual cyclone case from data collected and analyzed at the Naval Postgraduate School.

As with many studies, the results of this research has generated further questions and avenues for exploration. Although time limitations preclude more detailed analysis of the six-month correlation findings here, we recommend the following issues for future investigation:

1.   Further research is needed to classify the correlations by synoptic regime. Are particular synoptic regimes more conducive to higher correlations? Conversely, in what type of synoptic regime does the channel 3 MSU correlate poorly?

2.   Further study is needed to identify error sources that affect the processing and analysis of MSU brightness temperatures. Of particular interest are resolving the adverse effects of surface emission on the data and developing schemes to remove it, as well as the phasing problems induced by including "time-windowed" satellite data in single map-time analyses.

95

3.   Case studies, especially when model guidance is poor, should be performed to evaluate the efficacy of the MSU product.   Careful comparison of channel 3 MSU analyses with model analyses and forecasts might suggest conventional analysis deficiences and lead to the direct incorporation of channel 3 MSU data in numerical data-assimilation schemes.

4.   Use of the Naval Postgraduate School local collection and processing system should continue.   This will enable a "test" platform for evaluation of the usefulness of locally-collected channel 3 MSU to accurately monitor the local environment, especially over data-sparse areas such as the Eastern Pacific. Careful inspection of this real-time data for errors must also be performed.   Finally, methods to streamline the processing should be developed to enable the product to be transitioned to operational use by military forecasters.

LIST OF REFERENCES

Bell, G. D., and L. F. Bosart, 1993: A case study of diagnosis of the formation of an upper-level cutoff cyclonic circulation over the Eastern United States. *Mon. Wea. Rev.*, **121**, 1635-1655.

Bleck, R., 1973: Numerical forecasting experiments based on the observation of potential vorticity on isentropic surfaces. *J. Appl. Meteor.*, **12**, 737-752.

_____, 1974: Short range prediction in isentropic coordinates with filtered and unfiltered numerical models. *Mon. Wea. Rev.*, **102**, 813-829.

Bleck, R., and C. Mattocks, 1984: A preliminary analysis of the role of potential vorticity in Alpine lee cyclogenesis. *Beitr. Phys. Atmos.*, **57**, 357-368.

Carlson, T. N., 1991: *Mid-Latitude Weather Systems*. Harper Collins Academic, London, 507 pp.

Davis, C. A., and K. A. Emanuel, 1991: Potential vorticity diagnostics of cyclogenesis. *Mon. Wea. Rev.*, **119**, 1929-1953.

Errico, Ronald M., 1985: Spectra computed from a limited area grid. *Mon. Wea. Rev.*, **113**, 1554-1562.

Ertel, H., 1942: Ein Neuer hydrodynamischer Wirbelsatz. *Met. Z.*, **59**, 271-281.

Fujita, T. T., 1986: Mesoscale classifications: Their history and their application to forecasting. In *Mesoscale Meteorology and Forecasting*, P. S. Ray (Ed.), American Meteorological Society, Boston, 18-34.

Godson, W. L., 1948: A new tendency equation and its application in the analysis of surface pressure changes. *J. Meteor.*, **4**, 281-291.

Grody, N. C., 1983: Severe storm observations using the microwave sounding unit. *J. Climate Appl. Meteor.*, **22**, 609-625.

Hardy, R. L., 1971: Multiquadric equations of topography and other irregular surfaces. *J. Geophys. Res.*, **76**, 1905-1915.

97

Hirschberg, P. A., and J. M. Fritsch, 1991a: Tropopause undulations and the development of extratropical cyclones. Part I: Overview and observations from a cyclone event. *Mon. Wea. Rev.*, **119**, 496-517.

_____, and _____, 1991b: Tropopause undulations and the development of extratropical cyclones. Part II: Diagnostic analysis and conceptual model. *Mon. Wea. Rev.*, **119**, 518-550.

_____, and _____, 1993a: A study of the development of extratropical cyclones with an analytic model. Part I: The effects of stratospheric structure. *J. Atmos. Sci.*, **50**, 311-327.

_____, and _____, 1993b: On understanding height tendency. *Mon. Wea. Rev.*, **121**, 2646-2661.

_____, and _____, 1994: A study of the development of extratropical cyclones with an analytic model. Part II. Sensitivity to tropospheric structure and analysis of the height tendency dynamics. *Mon. Wea. Rev.*, **121**, 2312-2330.

Hirschberg, P. A., and J. D. Doyle, 1994: An examination of pressure tendency mechanisms in an idealized simulation of extratropical cyclogenesis, *Tellus (in press)*.

Holton, J. R., 1979: *An Introduction to Dynamic Meteorology*. Academic Press, New York, 391 pp.

Hoskins, B. J., M. E. McIntyre and A. W. Robertson, 1985: On the use and significance of isentropic potential vorticity maps. *Quart. J. Roy. Meteor. Soc.*, **111**, 877-946.

Hoskins, B. J., and P. Berrisford, 1988: A potential vorticity perspective of the storm of 15-16 October 1987. *Weather*. **43**, 122-129.

Jusem, J. C., and R. Atlas, 1991: Diagnostic evaluation of numerical model simulations using the tendency equation. *Mon. Wea. Rev.*, **119**, 2936-2955.

Keyser, D., and M. A. Shapiro, 1986: A review of the structure and dynamics of upper-level frontal *zones. Mon. Wea. Rev.*, **114**, 452-499.

Kidder, S. Q., and T. H. Vonder Haar, 1994: *Satellite Meteorology: An Introduction*, To be published by Academic Press.

Koehler, T. L., 1989: Limb correction effects on TIROS-N microwave sounding unit observations. *J. Appl. Meteor.*, **28**, 807-817.

Le Marshall, J. F., and A. J. Schreiner, 1985: Limb effects in satellite temperature sounding. *J. Climate Appl. Meteor.*, **24**, 287-290.

Machta, L., and E. Hughes, 1970: Atmospheric oxygen in 1967 to 1970. *Science*, **168**, 1582-1584.

Meeks, M. L., and A. E. Lilley, 1963: The microwave spectrum of oxygen in the earth's atmosphere. *J. Geophys. Res.*, **68**, 1683-1703.

Murakami, M., 1979: Large-scale aspects of deep convective activity over the GATE area. *Mon. Wea. Rev.*, **107**, 994-1012.

Nuss, W. A., and D. W. Titley, 1994: Use of multiquadric interpolation for meteorological objective analysis. *Mon. Wa. Rev.*, **122**, 1611-1631.

Orlanski, I., 1975: A rational subdivision of scales for atmospheric processes. *Bull. Amer. Meteor. Soc.*, **56**, 527-530.

Petterssen, S., 1956: *Weather Analysis and Forecasting*, 2d ed., McGraw-Hill, 428 pp.

Rao, P. K., 1990: *Weather Satellites*. American Meteorological Society, Boston. 503 pp.

Rossby, C. G., 1940: Planetary flow patterns in the atmosphere. *Quart. J. Roy. Meteor. Soc.*, **66**, Suppl. 68-87.

Spencer, R. W., J. R. Christy, and N. C. Grody, 1990: Global atmospheric temperature monitoring with satellite microwave measurements: Method and results, 1979-84. *J. Climate*, **3**, 1111-1128.

Spencer, R. W., W. M. Lapenta, and F. R. Robertson, 1994: Vorticity and vertical motions diagnosed from satellite deep layer temperatures. *Mon. Wea. Rev.* (In publication)

99

Uccellini, L. W., D. Keyser, K. F. Brill and C. H. Wash, 1985: The President's Day cyclone of 18-19 February 1979: Influence of upstream trough amplification and associated tropopause folding on rapid cyclogenesis. *Mon. Wea. Rev.*, **113**, 962-988.

Velden, C. S. 1992: Satellite-based microwave observations of tropopause-level thermal anomalies: Qualitative applications in extratropical cyclones events. *Wea. Forecasting*, **7**, 669-682.

Werbowetski, A., Ed., 1981: *Atmospheric sounder users guide.* NOAA Tech. Rep. NESS 83. U. S. Department of Commerce/NOAA/NESS, 82 pp. (NTIS PB81 230476.).

Yates, W., and A. Bateman, 1989: *Digital Signal Processing Design.* Computer Science Press, Rockville, MD., 345 pp.

INITIAL DISTRIBUTION LIST

		No. Copies
1.	Defense Technical Information Center Cameron Station Alexandria, Virginia 22304-6145	2
2.	Library, Code 52 Naval Postrgaduate School Monterey, California 93943-5101	2
3.	Oceanography Department Code OC/CO Naval Postgraduate School 589 Dyer Rd Rm 252 Monterey CA 93943-5122	1
4.	Meteorology Department Code MR/Hy Naval Postgraduate School 589 Dyer Rd RM 252 Monterey CA 93943-5114	1
5.	Dr. Paul A. Hirschberg Code MR/Hs Naval Postgraduate School 589 Dyer Rd RM 233 Monterey CA 93943-5114	4
6.	Dr. C. H. Wash Code MR/Wx Naval Postgraduate School 589 Dyer Rd RM 249 Monterey CA 93943-5114	3
7.	LT Matthew C. Parke, USN NAVLANTMETOC DET P.O. Box 9048, NAS Key West FL 33040-9048	1
9.	Mr. Eric Thalyer National Weather Service 10230 Smith Rd Denver, CO 80239	1

10. Dr. Roy Spencer
    Earth System Science Division
    NASA Marshall Space Flight Center
    Huntsville, AL 35812   1

11. Dr. LeRoy Spayd
    National Weather Service
    Services Evaluation Branch
    W/OM21
    1325 East-West Highway
    Silver Spring MD 20910   1

12. Dr. Louis Uccellini
    Director
    Office of Meteorology
    U. S. Department of Commerce
    National Oceanic and Atmospheric Administration
    National Weather Service
    Silver Springs, MD 20910   1

13. Dr. Kim Richardson
    Naval Research Laboratory
    7 Grace Hopper Avenue Stop 2
    Monterey CA 93943-5502   1

14. Commander
    Naval Oceanography Command
    Stennis Space Center
    MS 39529-5000   1

15. Commanding Officer
    Naval Oceanographic Office
    Stennis Space Center
    MS 39529-5001   1

16. Commanding Officer
    Fleet Numerical Meteorology and
    Oceanography Center
    7 Grace Hopper Ave Stop 4
    Monterey CA 93940-0001-0120   1

17. Commanding Officer
    Naval Oceanographic and Atmospheric
    Research Laboratory
    Stennis Space Center
    MS 39529-5004   1

102

18. Superintendent   1
    Naval Research Laboratory
    7 Grace Hopper Avenue Stop 2
    Monterey CA 93943-5502